

CRACK PROBLEMS IN GRADED COATINGS

**Bora Yildirim
and
Fazil Erdogan**

**Lehigh University
Bethlehem, PA 18015**

March 2001

**Air Force Office of Scientific Research
Grant F49620-98-1-0028**

DISTRIBUTION STATEMENT A
Approved for Public Release
Distribution Unlimited

20010419 099

DTIC CONVERSATION RECORD FOR DISTRIBUTION STATEMENT REQUEST

DTIC Personnel Making Call

TALK RIKE

Date

17 April 02

Time

1430

Authorizing Official

F. Erdogan

Phone

Agency

LEHIGH UNIV. MECH. Engineering : Mechanics

Title

Internet Document URL (if applicable)

Distribution Statement (Please check one box)

- ☒ DISTRIBUTION STATEMENT A: Approved for public release. Distribution is unlimited.
- ☐ DISTRIBUTION STATEMENT B: Distribution authorized to U.S. Government Agencies only.
- ☐ DISTRIBUTION STATEMENT C: Distribution authorized to U.S. Government Agencies and their contractors.
- ☐ DISTRIBUTION STATEMENT D: Distribution authorized to U.S. Department of Defense (DoD) and U.S DoD contractors only.
- ☐ DISTRIBUTION STATEMENT E: Distribution authorized to U.S. Department of Defense (DoD) components only.
- ☐ DISTRIBUTION STATEMENT F: Further dissemination only as directed by the controlling DoD office indicated below or by higher authority.
- ☐ DISTRIBUTION STATEMENT X: Distribution authorized to U.S. Government agencies and private individuals or enterprises eligible to obtain export-controlled technical data in accordance with DoD Directive 5230.25, Withholding of Unclassified Technical Data from Public Disclosure, 6 Nov 84.

Reason for the above identified distribution statement (in accordance with DoD Directive 5230.24)

Controlling Office

Date of Distribution Statement Determination

AQ Number (For DTIC-OCA Use Only)

CRACK PROBLEMS IN GRADED COATINGS

Bora Yildirim and Fazil Erdogan

ME-MECH. Department, Lehigh University, Bethlehem, PA 18015

Abstract

In this report a two-dimensional finite element technique is developed to study various mechanical, thermal and fracture mechanics problems encountered in the failure analysis of thermal barrier coatings. The system considered consists of the substrate, bond coat, thermally grown oxide and the top coat. The fracture problems studied include edge debonding, surface cracking, T-shaped cracks and periodic debond cracks along the bond coat / thermally grown oxide interface. The results obtained are mostly the stress intensity factors and the strain energy release rate. The enriched finite elements at and near the crack tip are used to simulate the asymptotic stress fields and to calculate the stress intensity factors.

1. Introduction

In many high temperature applications such as advanced turbine systems and earth-to-orbit winged planes, to achieve higher efficiencies, higher velocities and longer lifetime the use of structural ceramics is becoming a necessity for the protection of hot section components. The ceramic thermal barrier coatings used for these purposes, however, have some reliability and durability problems arising largely from high residual and thermal stresses, poor interfacial bonding strength and low coating toughness. Thus, the broader technical issues that need to be addressed in the development of thermal barrier coatings are the improvement of processing techniques from both performance and economic viewpoints, investigation of primary modes of failure, development of testing procedures for mechanical and strength characterization of the coatings and the development of appropriate life prediction methodologies [1, 2].

Because of the susceptibility of conventional homogeneous coatings to cracking and spallation, recently the materials research community has been exploring the possibility of new concepts in coating design. One such concept which may be used to overcome some of these shortcomings would be the introduction of an interfacial zone with graded thermomechanical properties between the coating and bond coat or the replacement of the coating by a composite layer with a volume fraction varying between 0% ceramic and 100% metal on the interface and 100% ceramic and 0% metal near the surface. Such particulate composites with continuously varying volume fractions are called *functionally graded materials (FGMs)* (see [3]-[6] for review and recent developments). The application of FGMs as coatings or interfacial zones seems to reduce the magnitude of residual stresses [7] and increase the bonding strength [8]. In FGM

coatings, because of the gradual increase of the metal content in the thickness direction, the toughness of the medium would also increase, thereby providing the layered material with a natural *R*-curve behavior.

In conventional ceramic coatings, even though one encounters a wide variety of failure modes, it is the interfacial fracture leading to spallation, which ultimately limits their performance. Both conventional and FGM thermal barrier coatings require a bond coat along the interface to shield the substrate against oxidation. In this report, the edge and T-shaped cracking of axisymmetric and plane strain specimens of finite dimensions with stress-free ends subjected to a uniform temperature change are considered. The effect of an oxide layer and interface undulations will also be studied but large deformation and rotation effects will be neglected.

2. Numerical Modeling of An Edge Crack parallel to Thermal Barrier Coating under Uniform Thermal Loading

In this section the axisymmetric crack problem for thermal barrier coatings (TBC) under a uniform temperature change is considered Figure 1. It is assumed that the disk-shaped specimen consists of a nickel-based super alloy substrate, NiCrAlY bond coat and the top coat. The top coat itself is a two phase metal/ceramic functionally graded material (FGM). The metal phase is NiCrAlY and the ceramic is partially stabilized zirconia (PSZ). The composition of top coat varies from zero percent ceramic on the bond coat/TBC interface to one hundred percent on the surface. The crack is a plane edge crack, starts at $r=r_0$ and propagates in a plane perpendicular to the axis of the cylinder, r_0 being the radius of the disk. Modes I and II stress intensity factors and the strain energy

release rate are calculated for various sizes and locations of the crack. The main variables in the problem are the inhomogeneity parameters of the FGM coating, the size and the location of the crack and the relative dimensions of the specimen. The finite element method is used to solve the problem. The material property grading is accounted for by developing special inhomogeneous elements and the stress intensity factors are calculated by using enriched crack tip elements [9].

The axisymmetric problem considered is described in Figure 1. The medium is free of any mechanical constraints and a uniform temperature change $+\Delta T$ causes the only nonvanishing load.

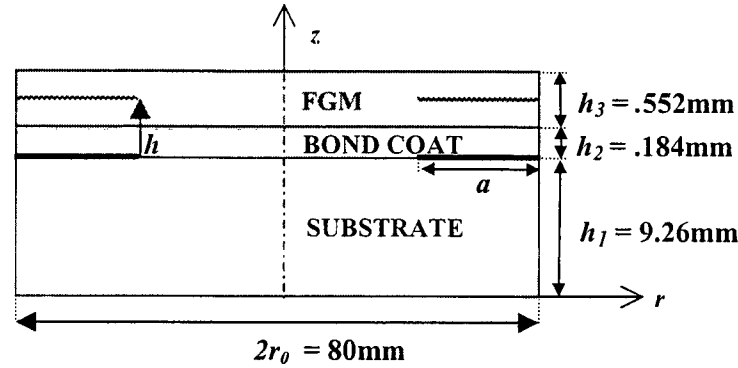


Figure 1: Geometry of the medium(Circular disk) .

At reference temperature T_0 the bonded medium is assumed to be stress-free. The volume fraction of ceramic in the FGM coating is varied from 0% on the bond coat/coating interface at $z = h_1 + h_2$ to 100% on the surface, at $z = h_1 + h_2 + h_3$. The following models are used to represent the thickness variation of the thermoelastic parameters in the coating:

$$E(z) = \begin{cases} E_s & , z \leq h_1 \\ E_{bc} & , h_1 < z \leq h_1 + h_2 \\ E_c + (E_{bc} - E_c) \left(\frac{h_1 + h_2 + h_3 - z}{h_3} \right)^{p_1} & , h_1 + h_2 < z \leq h_1 + h_2 + h_3 \end{cases} \quad (1)$$

$$\alpha(z) = \begin{cases} \alpha_s & , z \leq h_1 \\ \alpha_{bc} & , h_1 < z \leq h_1 + h_2 \\ \alpha_c + (\alpha_{bc} - \alpha_c) \left(\frac{h_1 + h_2 + h_3 - z}{h_3} \right)^{p_2} & , h_1 + h_2 < z \leq h_1 + h_2 + h_3 \end{cases} \quad (2)$$

$$v(z) = \begin{cases} v_s & , z \leq h_1 \\ v_{bc} & , h_1 < z \leq h_1 + h_2 \\ v_c + (v_{bc} - v_c) \left(\frac{h_1 + h_2 + h_3 - z}{h_3} \right)^{p_3} & , h_1 + h_2 < z \leq h_1 + h_2 + h_3 \end{cases} \quad (3)$$

where subscripts s , bc and c stand for substrate, bond coat and ceramic, respectively and p_i ($i=1,2,3$) is the inhomogeneity constant, $0 < p_i < \infty$. From (1)-(3) it may be seen that the limiting cases $p_i=0$ and $p_i=\infty$ correspond to homogeneous top coat having the properties of bond coat and ceramic, respectively. By adjusting this constant the ceramic-rich ($p_i > 1$) and metal rich ($p_i < 1$) compositions in the FGM coating may be simulated. Figure 2 shows a sample variation of the Young's modulus for various values of $p_i=p$.

The thermoelastic material properties of ceramic, bond coat and substrate are given in Table 1, where E , ν and α are Young's modulus, Poisson's ratio and thermal expansion coefficient, respectively. The material properties are known at three different temperatures [10]. Consequently, a best fit to the data appears to be a second degree polynomial for $E(T)$ and $\alpha(T)$ and a bilinear function for $\nu(T)$ (Figures 3-5).

The main results presented in this study are modes I and II stress intensity factors, K_I , K_{II} and the strain energy release rate G which are normalized with respect to (see Figure 1 and Equation 1)

$$K_0 = E_s \alpha_s \Delta T \sqrt{\pi h_3}, \quad G_0 = (1 - \nu_s^2) \frac{K_0^2}{E_s}. \quad (4)$$

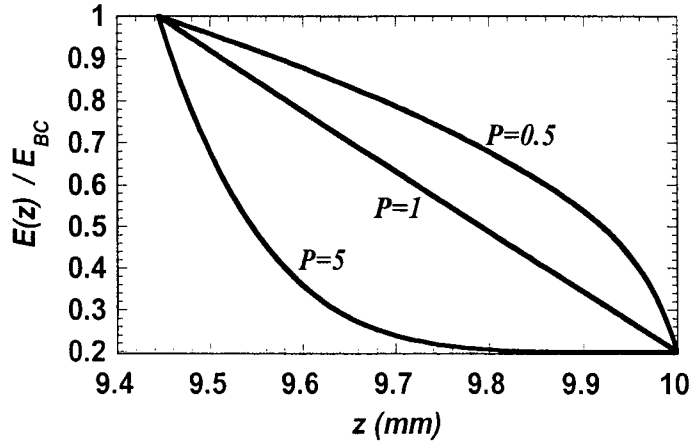


Figure 2: Variation of Young's modulus in the FGM coating.

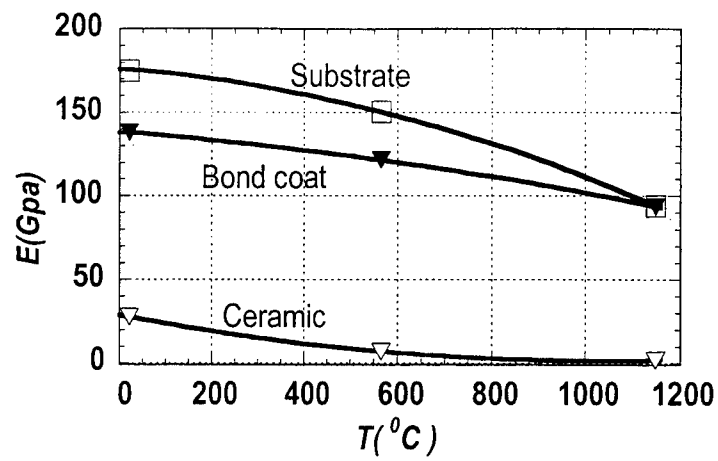


Figure 3: Variation of Young's modulus as a function of temperature.

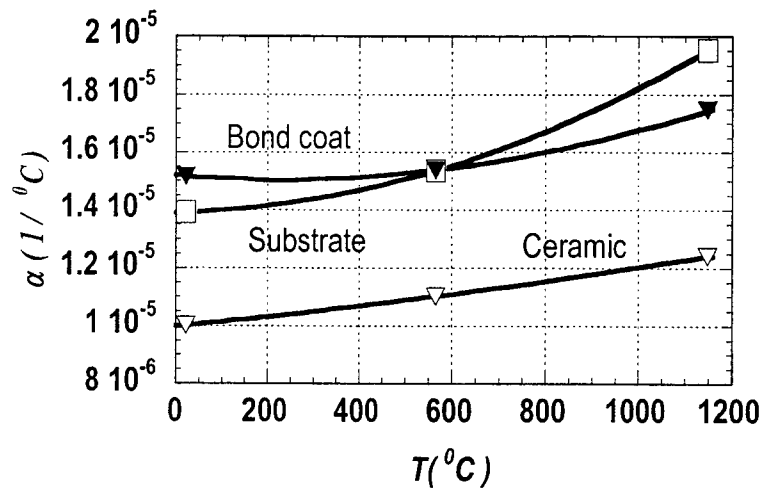


Figure 4: Variation of thermal expansion coefficient as a function of temperature.

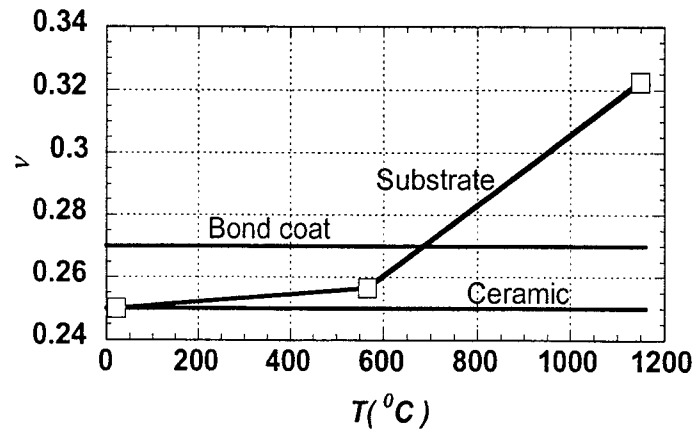


Figure 5: Variation of Poisson's ratio as a function of temperature.

In the examples shown in Figures 6-8 the stress intensity factors and the strain energy release rate are given as functions of the crack distance h for a fixed crack length $a=h_3$ and for various values of the inhomogeneity constant p . Note that at $h=0$, for all p , and at $h=h_2$, for $p=\infty$, the crack lies along a bimaterial interface. Consequently, the stress singularity is complex, K_I and K_{II} are discontinuous but, as expected, G is continuous. Similar results are shown in Figures 9-11 for a crack length $a=h_3/2$. On physical grounds the following observations may be made: In the composite medium under consideration for a uniform change in temperature the stresses are generated by the mismatch in the thermal expansion coefficients and the net ligament stresses in the crack plane are statically self-equilibrating. Therefore, as the crack plane approaches the free surface, that is for $h \rightarrow h_2+h_3$ (or noting that, since $h_3=3h_2$, for $h \rightarrow 4h_2$), the stress intensity factors and the strain energy release rate tend to zero, which is seen to be the case in Figures 6-11. The figures also show that for the values of a/h_3 considered, K_I , K_{II} and G are not significantly influenced by the crack length. From equation 4 and Figures 6 and 9 it may be seen that $K_I > 0$ for $\Delta T > 0$. Also Figures 7 and 10 show that as h increases K_{II} changes sign at a critical value $h=h_{cr}$, $K_{II} > 0$ for $0 < h < h_{cr}$ and $K_{II} < 0$ for $h_{cr} < h < h_2+h_3$. If K_{II} is nonzero, then the stress state around the crack tip is one of mixed mode and, unless the plane of the crack is a weak cleavage plane, the crack propagation cannot be coplanar. In this case the crack path would deviate at an angle determined by the sign of K_{II} and relative magnitudes of K_I and K_{II} . This is qualitatively shown in Figure 12. The important physical conclusion here is that for a given FGM (or value of p), since the magnitudes of K_I and K_{II} are relatively independent of the crack length, $h=h_{cr}$ plane is a plane of stable crack growth. As physically expected, the figures also show that the magnitudes

of the strain energy release rate decrease as the metal content of the FGM coating increases.

As in any fracture problem, the path of the propagating crack is dependent on the crack driving force G and the material parameter G_c representing the crack growth resistance, Figures 8 and 11 indicate that for given a p , G is approximately maximum around $h=h_2$, that is, along the TBC/Bond Coat interface. If one also considers the fact that usually an oxide scale (normally Al_2O_3) forms along the top coat/bond Coat interface as the medium is exposed to high temperature over an extended period of time resulting in a plane of weak fracture resistance, it is reasonable to conclude that the crack propagation in the medium would be confined to a plane at or very near to the top coat/bond coat interface. Thus, in the next set of the results given in Figures 13-18 it is assumed that the crack lies along the top coat/bond coat interface, $h=h_2$. Again, because of the self equilibrating stress state in the medium, it is physically expected that the stress intensity factors K_I , K_{II} and the strain energy release rate G tend to zero as $a \rightarrow 0$ and $a \rightarrow r_0$. This is clearly seen to be the case in Figures 13-18. The results given in Figures 13-15 are calculated by using temperature-independent material properties corresponding to the

reference temperature T_0 (in this case, room temperature). The influence of the temperature dependence of the material properties (described in Figures 3-5) on K_I , K_{II} and G is shown in Figures 16-18. Figures 13-18 show that the effect of temperature dependence is very significant only in the case of a homogenous ceramic top coat ($p=\infty$). The reason for this appears to be excessive softening of the ceramic at high temperature (Figure 3) and the fact that G is inversely proportional to the overall stiffness.

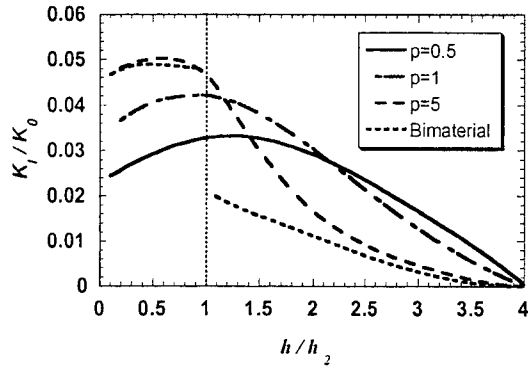


Figure 6: Mode I stress intensity factors vs. crack distance h for different coating types ($a=h_3$).

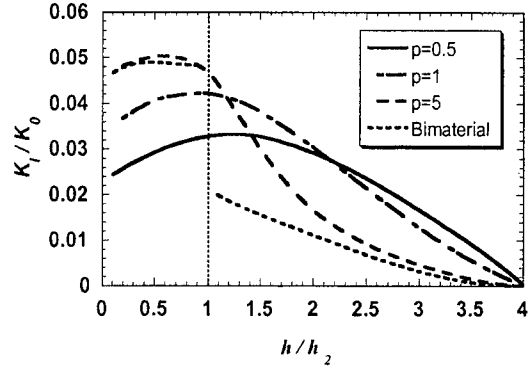


Figure 9: Mode I stress intensity factors vs. crack distance h for different coating types ($a=h_3/2$).

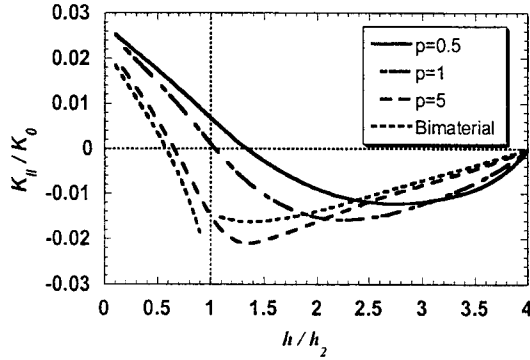


Figure 7: Mode II stress intensity factors vs. crack distance h for different coating types ($a=h_3$).

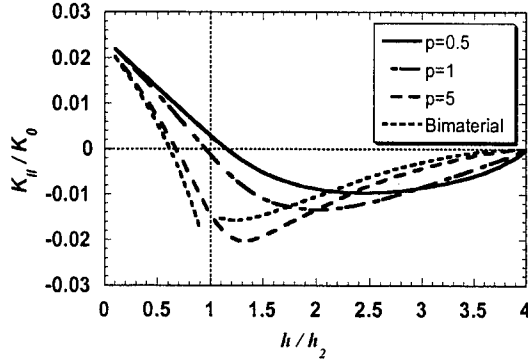


Figure 10: Mode II stress intensity factors vs. crack distance h for different coating types ($a=h_3/2$).

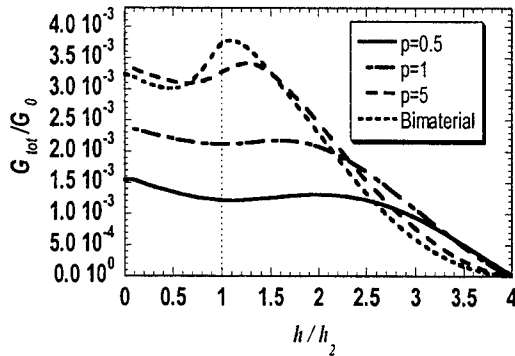


Figure 8: Strain energy release rates vs. crack distance h for different coating types ($a=h_3$).

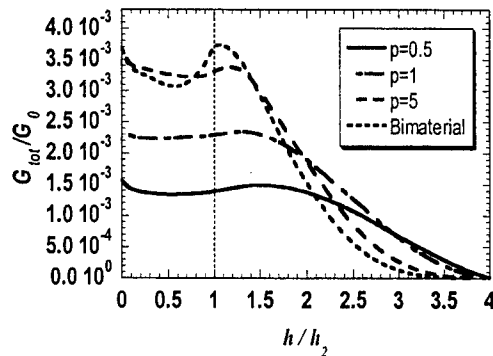


Figure 11: Strain energy release rates vs. crack distance h for different coating types ($a=h_3/2$).

For the edge crack considered, Figure 19 shows the deformed shape of the specimen and typical finite element mesh used in the study. Finite element formulation for FGM materials and enriched crack tip elements can be found in references [9] and [11].

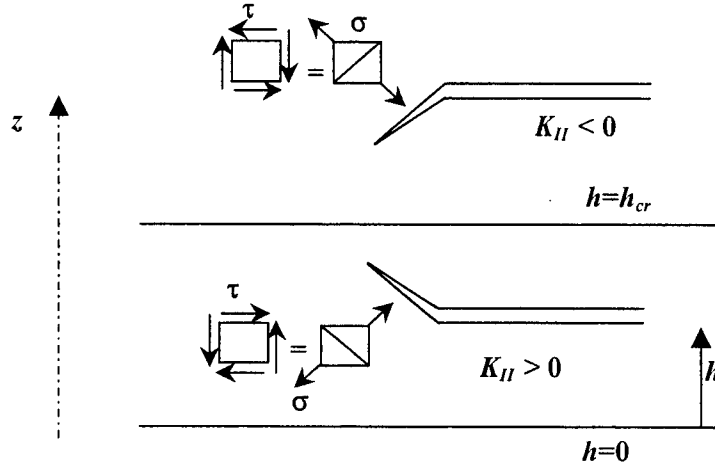


Figure 12: Stable crack growth plane $h=h_c$ and crack propagation direction above and below this plane.

Table 1: Material properties of a TBC system at 22, 566 and 1149 °C [10].

Material	E (GPa)	ν	α (°C ⁻¹)
Substrate	175.8	0.2500	13.91x10 ⁻⁶
	150.4	0.2566	15.36x10 ⁻⁶
	94.1	0.3224	19.52x10 ⁻⁶
Bond coat	137.9	0.27	15.16x10 ⁻⁶
	121.4	0.27	15.37x10 ⁻⁶
	93.8	0.27	17.48x10 ⁻⁶
Ceramic	27.6	0.25	10.01x10 ⁻⁶
	6.9	0.25	11.01x10 ⁻⁶
	1.84	0.25	12.41x10 ⁻⁶

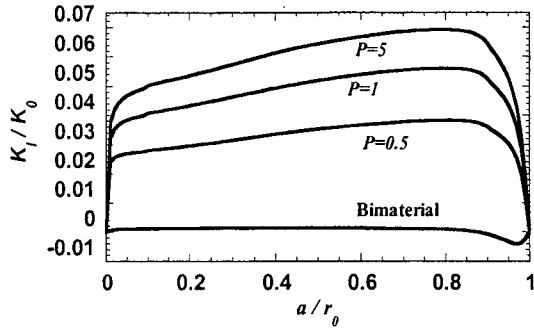


Figure 13: Mode I stress intensity factors vs crack length a for different coating types ($h=h_2$).

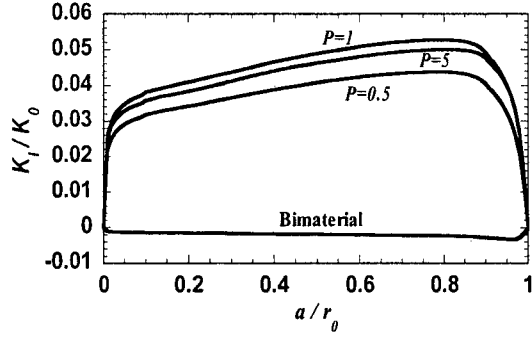


Figure 16: Mode I stress intensity factors vs. crack length a for different coating types ($h=h_2$ and temperature dependent thermoelastic properties used).

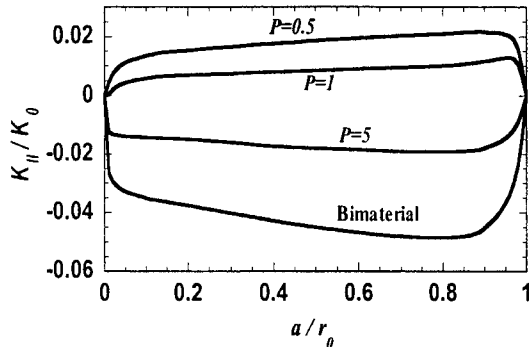


Figure 14: Mode II stress intensity factors vs. crack length a for different coating types ($h=h_2$).

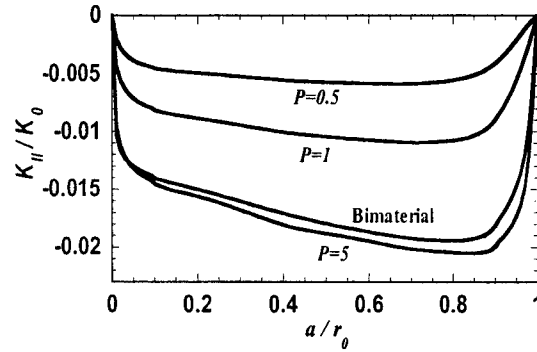


Figure 17: Mode II stress intensity factors vs. crack length a for different coating types ($h=h_2$ and temperature dependent thermoelastic properties used).

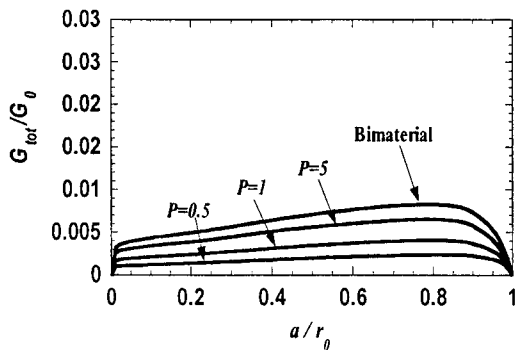


Figure 15: Strain energy release rates vs. crack length a for different coating types ($h=h_2$).

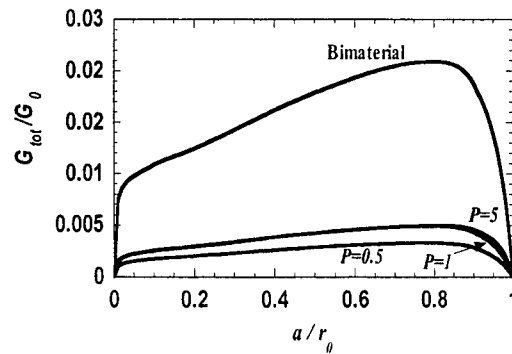


Figure 18: Strain energy release rates vs. crack length a for different coating types ($h=h_2$ and temperature dependent thermoelastic properties used).

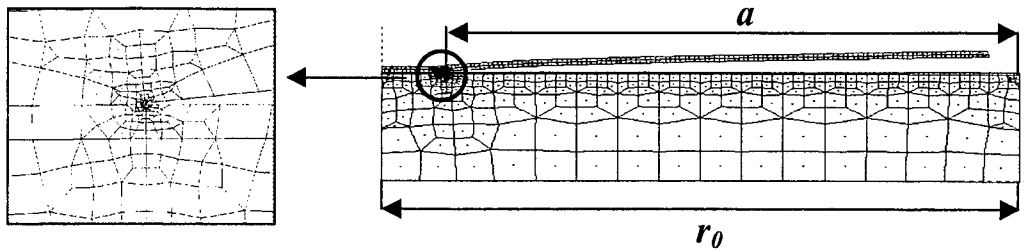


Figure 19: Deformed finite element mesh and a close up view of the crack tip elements.

3. An Edge Crack perpendicular to Thermal Barrier Coating without a TGO layer under Uniform Thermal Loading

The plane strain problem considered is described in Figure 1.20. The medium is free of any mechanical constraints, and a uniform temperature change $+\Delta T$ is the only nonvanishing load. The medium is assumed to be stress free at the ambient temperature T_0 .

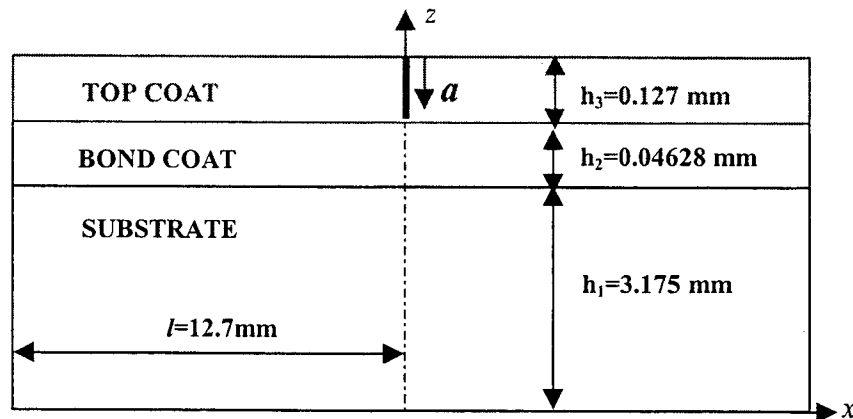


Figure 20: Geometry used in edge crack-TBC problem without TGO.

An edge crack propagating perpendicular to the layers is modeled. The crack starts on the surface of the top coat, it then propagates through the top coat and bond coat (perpendicular to the interfaces) into the substrate. The strain energy release rates are calculated as a function of the crack length. Since the geometry is symmetric and loading is uniform, there is no mode II stress intensity factor. For the top coat, a model of different FGM coatings and a homogenous ceramic coating have been used. For FGM coatings, the model described by equations eqs. 1-3, has been used and, it is assumed that $p_1 = p_2 = p_3 = p$. The results are given in Figure 21 which are calculated by using temperature-independent material properties (see Table 1) corresponding to the

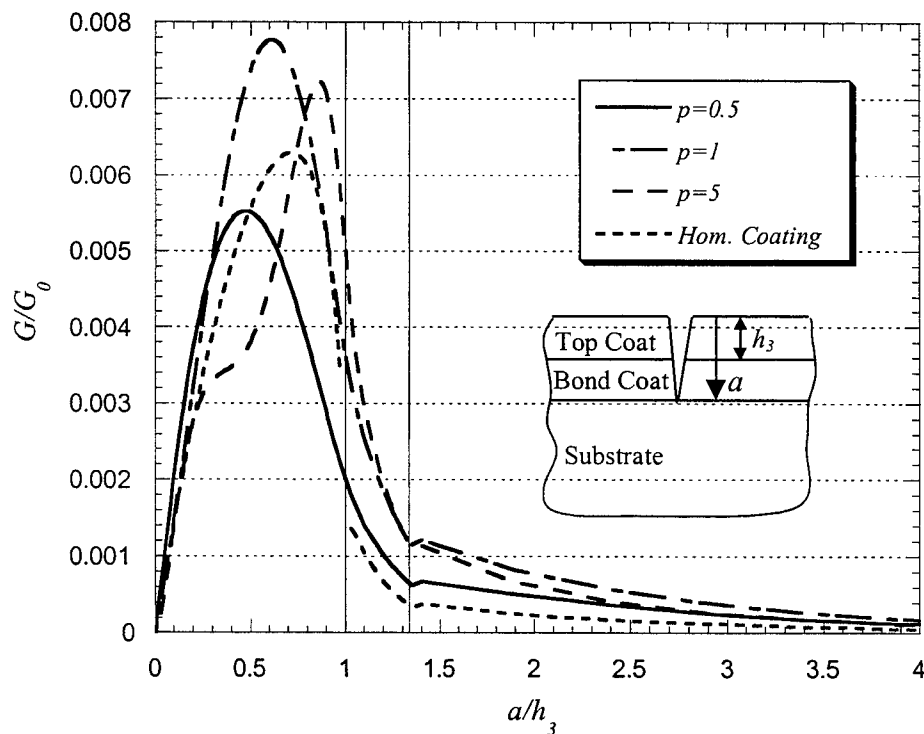


Figure 21: Strain energy release rates vs. crack length a for different coating types.

reference temperature T_0 (in this case, room temperature) for homogenous top coat and equations 1-3 for FGM coatings. G_0 is defined by equation 4. In total, thirty crack lengths were used to plot the curves for each coating type simulated. Examining Figure 21, it can be seen that maximum strain energy release rates occur in the zone defined by the graphs. As expected, the metal rich top coat ($p < 1$) has the lowest peak and, unexpectedly, the linear type top coat ($p = 1$) has the highest peak. The ceramic rich coating ($p = 5$) has a lower peak than metal rich but higher peak than the homogenous coating. Close to the top coat/bond coat interface, strain energy release rates decrease rapidly. For the homogeneous case, the curve is discontinuous at the interface ($a = h_3$). There is a sudden decrease in strain energy release rates as the crack tip approaches the top coat/bond coat interface, this decrease continues as the crack goes into substrate and finally goes to zero when the crack tip reaches the free surface of the substrate.

4. An Edge Crack perpendicular to the Thermal Barrier Coating with TGO under Uniform Thermal Loading

As mentioned in previous sections, the current design of TBC's consists of a partially stabilized zirconia coating deposited on an intermediate metallic bond coat (e.g., NiCrAlY), which is plasma sprayed on the (superalloy) substrate (see Figure 22). The main function of the bond coat is to protect the substrate against oxidation. At high temperatures a thermally grown oxide (TGO) layer, (usually an Al_2O_3 scale) is formed along the PSZ-bond coat interface. Even though this Al_2O_3 layer forms an oxygen diffusion barrier, it also introduces a weak cleavage plane, which under thermal cycling, may lead to spallation. One of the major problems in the failure of thermal barrier coatings is the spallation of the coating. The newly produced oxide layer has a very high

elastic modulus and distinct material properties. Therefore, very high residual stresses may develop in this layer during thermal cycling and may lead to very high stress intensity factors, if there exists a crack. If an FGM top coat is used, this newly introduced oxide layer has a big effect on material property continuity through the thickness, because there is an extra layer of material (TGO) inserted between the top coat and bond coat. Material properties of TGO is shown in Table 2. In reality, the TGO-bond coat interface has an undulated shape, but here for simplicity, it is modeled as a plane interface and 10 microns is used as the thickness of this layer [12]. Geometry of the TBC considered in this section is shown in Figure 23, (not drawn to scale). It should be noted that because of the thinness of the oxide layer compared to other layers, some difficulties were encountered in finite element meshing. It was made to ensure that at least 5 cubic elements were used along the thickness of the oxide layer near the crack face. A sample mesh used in this study is shown in Figure 24. Since this extra layer of oxide changes the material property distribution along the thickness of the topcoat, a new formulation is necessary. The new material property distribution along the thickness can be written as follows (see Figure 23):

$$E(z) = \begin{cases} E_s & , z \leq h_1 \\ E_{bc} & , h_1 < z \leq h_1 + h_2 \\ E_{TGO} & , h_1 + h_2 < z \leq h_1 + h_2 + h_3 \\ E_c + (E_{bc} - E_c) \left(\frac{h_1 + h_2 + h_3 + h_4 - z}{h_3} \right)^{p_1} & , h_1 + h_2 + h_3 < z \leq h_1 + h_2 + h_3 + h_4 \end{cases} \quad (5)$$

$$v(z) = \begin{cases} v_s & , z \leq h_1 \\ v_{bc} & , h_1 < z \leq h_1 + h_2 \\ v_{TGO} & , h_1 + h_2 < z \leq h_1 + h_2 + h_3 \\ v_c + (v_{bc} - v_c) \left(\frac{h_1 + h_2 + h_3 + h_4 - z}{h_3} \right)^{p_2} & , h_1 + h_2 + h_3 < z \leq h_1 + h_2 + h_3 + h_4 \end{cases} \quad (6)$$

$$\alpha(z) = \begin{cases} \alpha_s & , z \leq h_1 \\ \alpha_{bc} & , h_1 < z \leq h_1 + h_2 \\ \alpha_{TGO} & , h_1 + h_2 < z \leq h_1 + h_2 + h_3 \\ \alpha_c + (\alpha_{bc} - \alpha_c) \left(\frac{h_1 + h_2 + h_3 + h_4 - z}{h_3} \right)^{p_3} & , h_1 + h_2 + h_3 < z \leq h_1 + h_2 + h_3 + h_4 \end{cases} \quad (7)$$

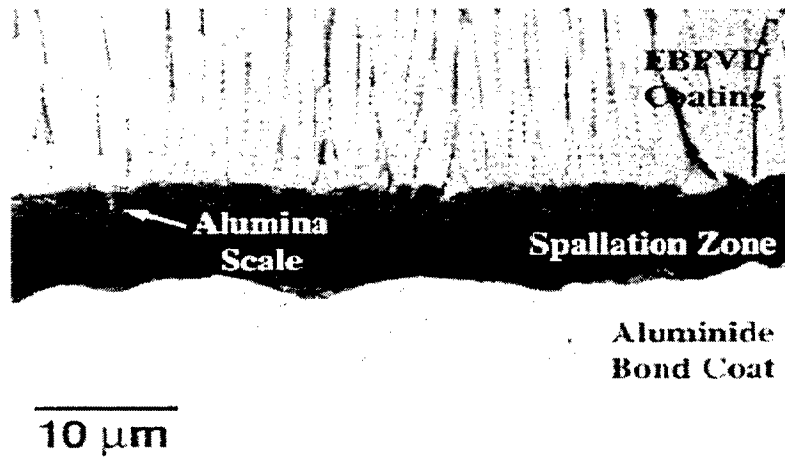


Figure 22: Cross-section of an EBPVD YSZ coating deposited on a superalloy substrate coated with an aluminide bond coat after exposure to oxidative environments[9].

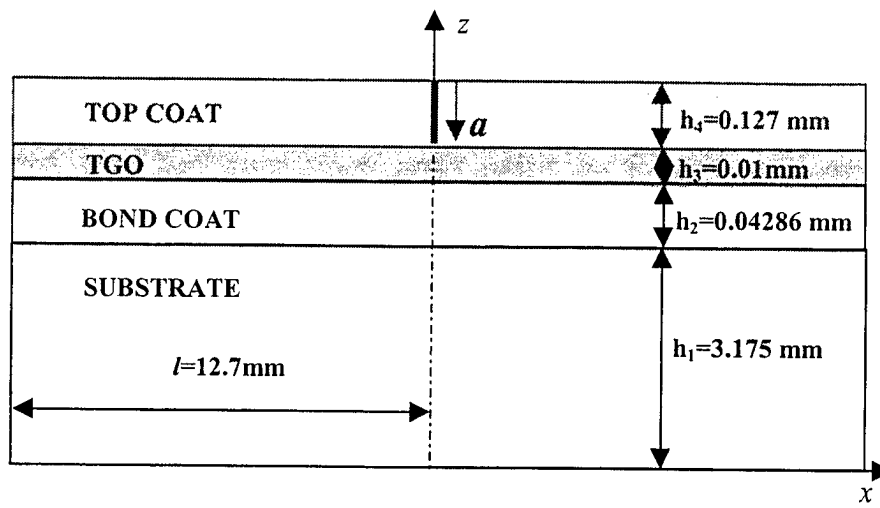


Figure 23: Geometry used in edge crack-TBC problem with TGO.

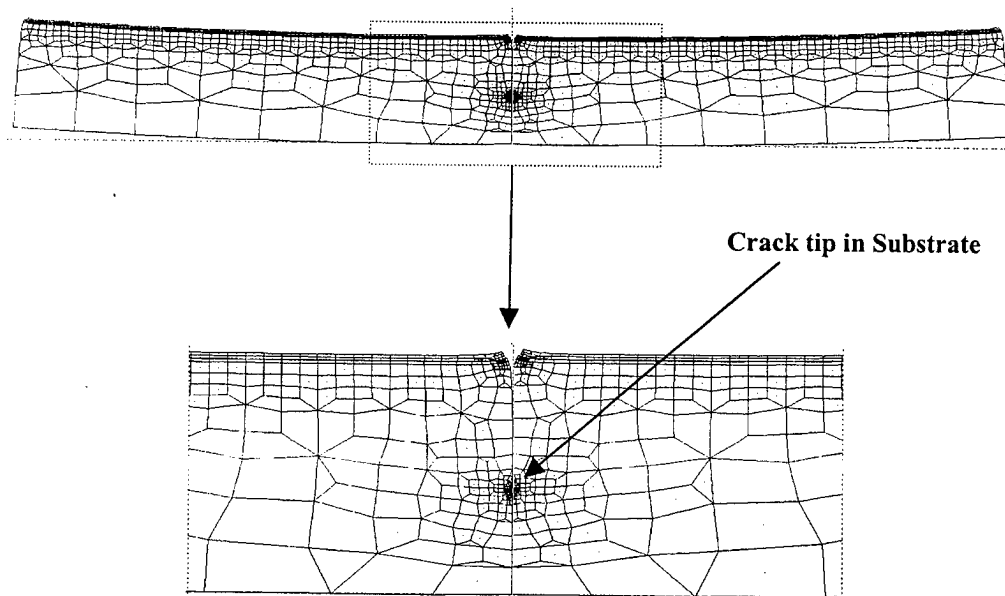


Figure 24: A sample mesh used in edge crack-TBC problem with TGO layer.

Table 2: Material properties of TGO.

Material	E (GPa)	ν	α ($^{\circ}\text{C}^{-1}$)
TGO	320	0.21	8.8×10^{-6}

$p_1=p_2=p_3=p$ is assumed in this study. Again, an edge crack is assumed to start at the surface of the top coat, eventually going through the top Coat, TGO, bond coat into the substrate (perpendicular to the surface). Strain energy release rates are calculated and plotted as a function of crack length. Since the thickness of the TGO is quite small, results are shown on a unscaled graph in Figure 25. This also is a Mode I problem because of the symmetric geometry, boundary conditions and uniform thermal loading. Comparing Figure 21 to Figure 25, it can be seen that introduction of the TGO does not have much effect on the behavior of strain energy release rates in the top coat for all coating types whereas it has changed the magnitude of strain energy release rates in bond coat and substrate. Maximum strain energy release rates occur in the TGO near the TGO/bond coat interface and both TGO interfaces may be weak fracture planes. Therefore, it appears that from a fracture view point TGO may be the critical layer. There may be two scenarios here. First, if the crack tip somehow reaches the TGO-top coat interface, the crack may suddenly propagate through the TGO. On the other hand, strain energy release rates decrease to zero at top coat/TGO interface. This means that the crack may be arrested before reaching the TGO layer. In the following section, the later scenario will be examined in detail.

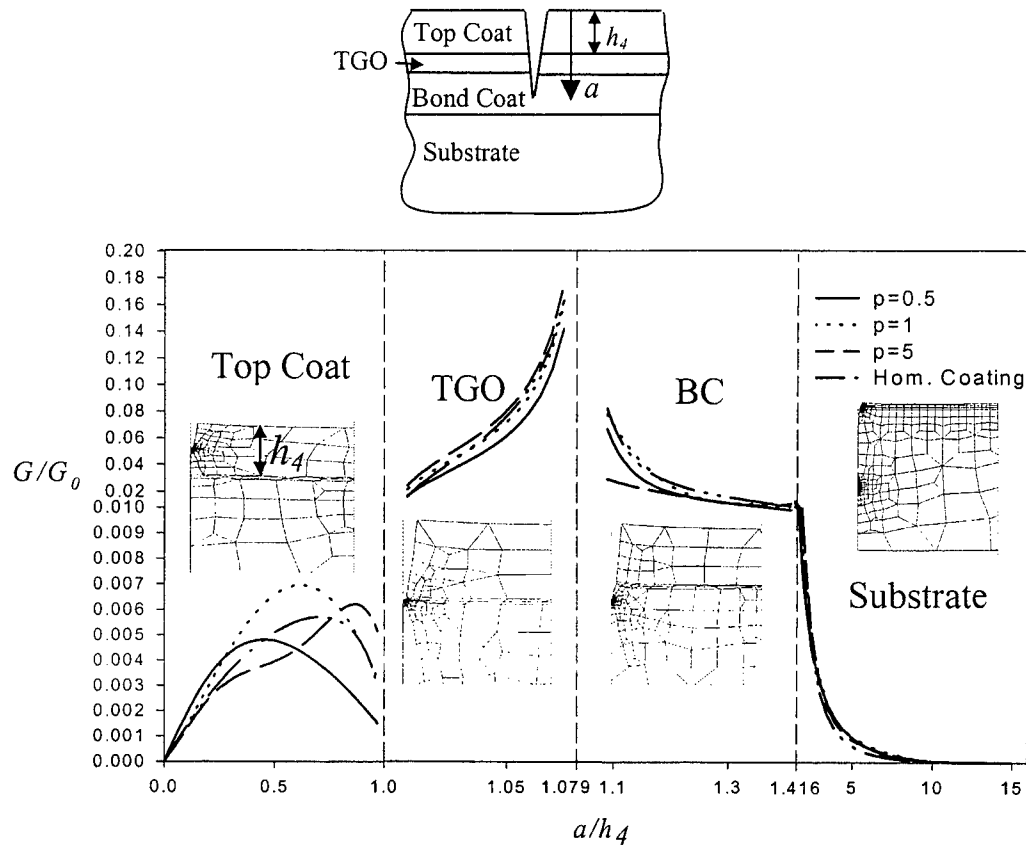


Figure 25: Strain energy release rates vs. crack length a for different coating types (TGO is included in the model),

$$K_0 = E_s \alpha_s \Delta T \sqrt{\pi h_4}, \quad G_0 = (1 - \nu_s^2) \frac{K_0^2}{E_s}.$$

5. T-shaped cracks in Thermal Barrier Coatings with TGO under Uniform Thermal Loading

As mentioned in the previous section, an edge crack propagating perpendicular to an oxide interface may either arrest at this interface due to decreasing strain energy rates or may continue to propagate into the oxide layer. If it is arrested at the interface, it may divert into two branches (due to weak cleavage planes at the top coat/TGO interface) and may become a T-shaped crack (see Figure 26).

The medium is free of any mechanical constraints, and a uniform temperature change $+\Delta T$ causes the only nonvanishing load. The medium is assumed to be stress free at the ambient temperature T_0 . A T-shaped crack that has branches propagating along the top coat/TGO interface is modeled. Geometry and dimensions used in this study are shown in Figure 26, which is not drawn to scale. Mesh refinement is used along the thickness of oxide layer at and near the branch-crack-tips (a typical mesh used in this analysis is shown in Figure 27). Because of the lack of symmetry, this problem is a mixed mode (I and II) problem. Here a is fixed and only b (half branch crack length) is varied. The strain energy release rate as a function of branch length, b has been calculated. The results obtained from these calculations are shown in Figure 28. As can be seen from Figure 28, the strain energy release rate is approximately constant for all branch lengths, (i.e. it is not a function of b) for all coatings and it decreases as b approaches the half length of the geometry studied (i.e., $b \rightarrow l$). The strain energy release rate increases as the ceramic content of the top coat increases (i.e., as p increases). The strain energy release rate obtained from a homogenous ceramic top coat fall in between that of the linear type ($p=1$) and metal rich ($p<1$) top coat. Although, the strain energy release rates are expected to vary smoothly as the volume fraction of ceramic in the FGM is varied between two limits, $0 \leq p \leq \infty$, Figure 28 shows a different trend due to the explanation in Section 1.4. If the TBC is examined carefully and equations (5)-(7) are reconsidered, it can be seen that as the oxide layer develops between top coat and bond coat, material property continuity along the thickness of top coat vanishes because of the distinct material properties of this newly grown layer.

Again an extension of this work is done by locating the crack branches between TGO/bond coat interface using the same geometry and loading. Results for this new case are shown in Figure 29. A rather interesting result was obtained from this second case. Magnitudes of strain energy release rates increase one order and strain energy release rates vary smoothly as the volume fraction of the ceramic in the FGM is varied between two limits, $0 \leq p \leq \infty$, i.e., $G_{p<1} < G_{p=1} < G_{p=5} < G_{p=\infty}$. This indicates that as long as the crack is located along the bond coat, an extra layer of TGO does not have much effect on the smooth variation of the strain energy release rates. Again, the strain energy release rates are constant for all branch lengths, (i.e. are not a function of b) for all types of coatings and decrease to zero as b approaches the half length of the geometry studied (i.e., $b \rightarrow l$).

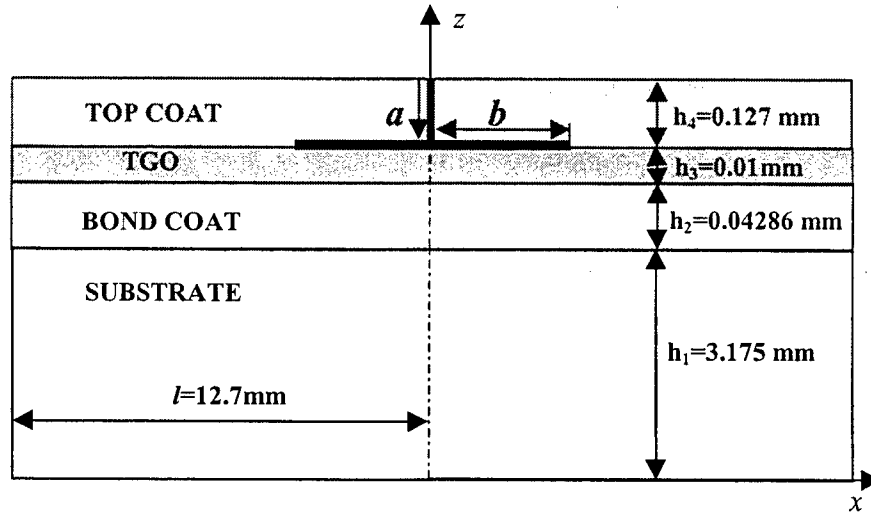


Figure 26: Geometry used in T-shaped cracked TBC problem with TGO.

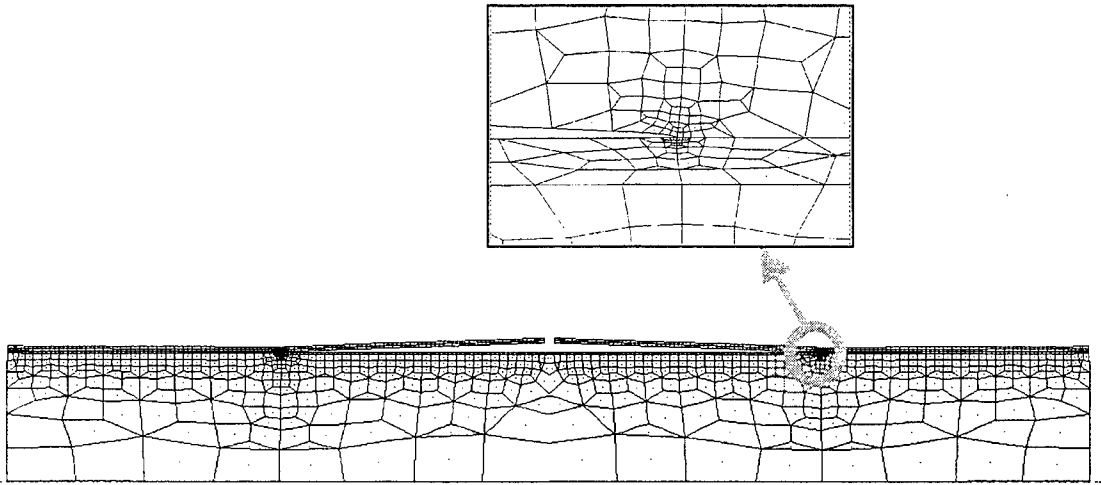


Figure 27: Finite element mesh used in T-shaped cracked TBC problem.

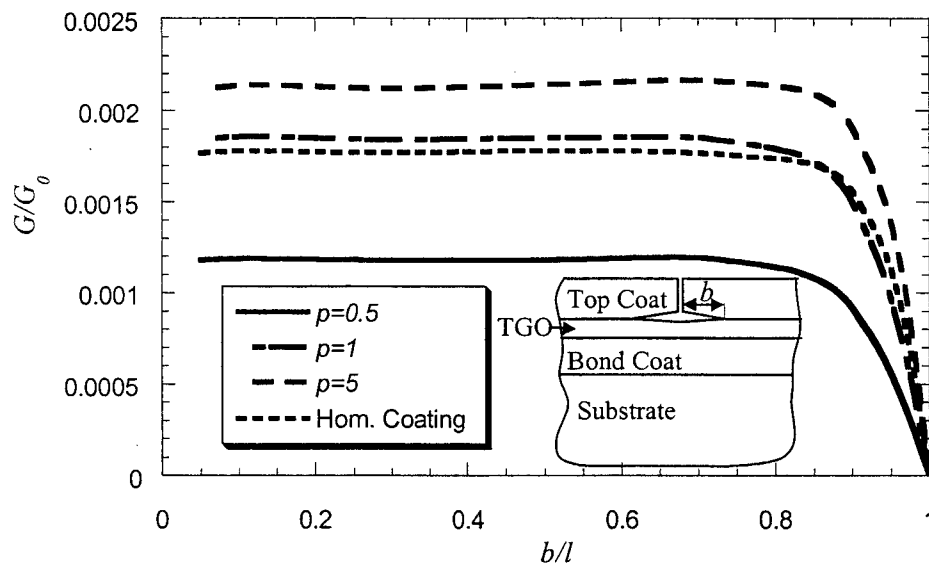


Figure 28: Strain energy release rates vs. crack branch length b for different coating types (TGO is included in the model),

$$K_0 = E_s \alpha_s \Delta T \sqrt{\pi h_4}, \quad G_0 = (1 - \nu_s^2) \frac{K_0^2}{E_s}.$$

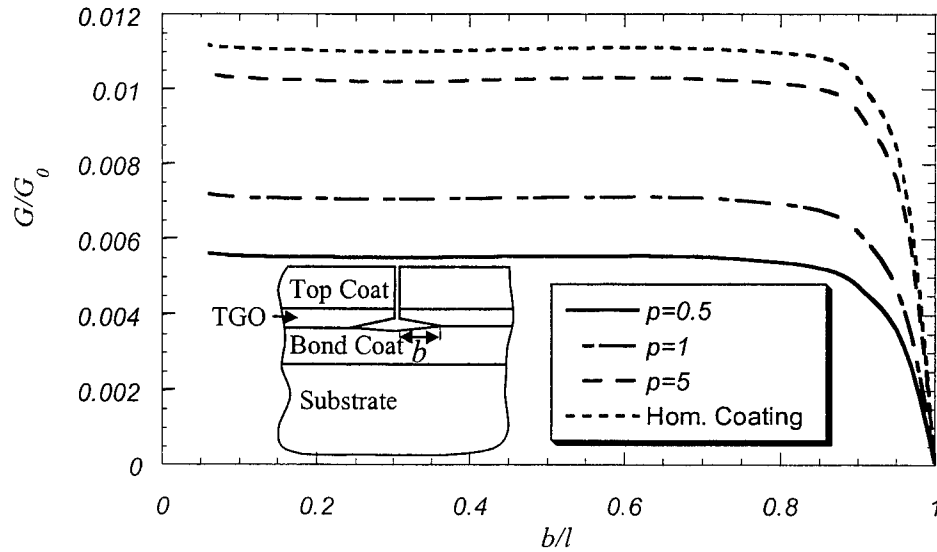


Figure 29: Strain energy release rates vs. crack branch length b for different coating types (TGO is included in the model),

$$K_0 = E_s \alpha_s \Delta T \sqrt{\pi h_4}, \quad G_0 = (1 - \nu_s^2) \frac{K_0^2}{E_s}.$$

6. Stress Calculations in TBCs Using Undulating Interface Model (both ends are constrained horizontally)

In actual TBC specimens, the oxide layer growing along top coat/bond coat interface usually has an undulated shape or wavy interface rather than a straight interface (see Figure 30 and reference[13]). In Sections (4-5) for simplicity, a plane interface was assumed. In this section, an undulated interface is modeled and the most likely crack location is determined by examining the maximum normal stresses along the bond coat/TGO and top coat/TGO interface.

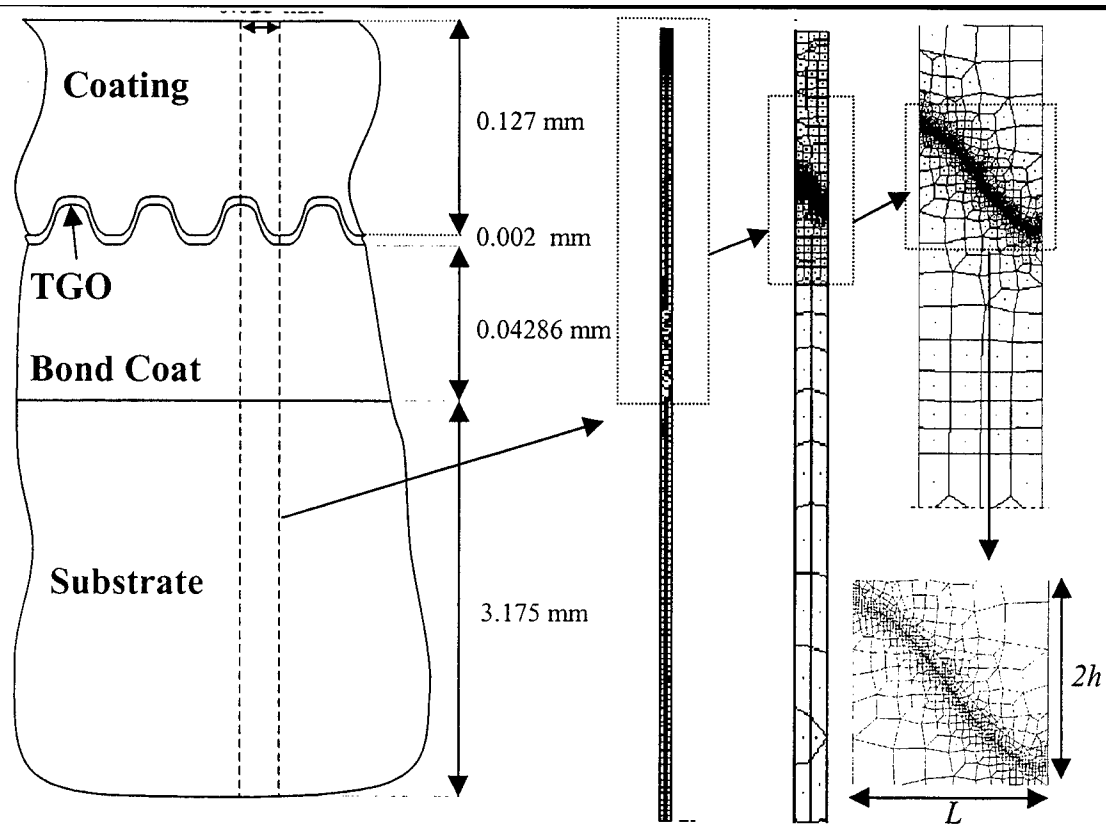


Figure 30: Geometry and Finite Element model used in undulation problems, $L=0.025$ mm $h=0.01$ mm.

A cosine wave interface model is used to simulate the rough bond coat/TGO and top coat/TGO interfaces. Equation 8 shows the cosine wave model used.

$$S(x) = \left\{ \begin{array}{l} 3.22786 + h \cos\left(\frac{\pi x}{L}\right), \text{TGO / Bond Coat interface} \\ 3.22986 + h \cos\left(\frac{\pi x}{L}\right), \text{TGO / Top Coat interface} \end{array} \right\} \quad (8)$$

where $0 \leq x \leq L=0.025$ mm and $h=0.01$ mm.

The same model were also created in ANSYS, two separate runs were performed, and the results are compared. The same material properties are used as in the previous sections (see Table 1 and Table 2). Geometry, boundary conditions and a typical mesh used for this analysis are shown in Figure 30. The wavelength, height and thickness of the undulations used in this analysis were taken from reference [14]. Symmetric

boundary conditions were used on both sides of the slice, i.e., both edges were constrained horizontally. $\Delta T = -1000^\circ\text{C}$ is the only nonvanishing load applied. Unlike previous cases, there is a temperature drop i.e., cool down from the processing temperature and at the processing temperature, specimen is assumed to be stress free. The stress distribution in the specimen is calculated. The comparison of results along two vertical edges of the slice is shown in Figures 31 and 32. As can be seen from these figures, σ_{xx} and σ_{yy} calculated along the symmetry lines is exactly the same as the ones calculated using ANSYS. Stress contours obtained from ANSYS are also illustrated in Figure 33 to give insight into the stress distribution over the slice. From these contour plots, we can also see that maximum σ_{xx} , σ_{yy} , σ_{xy} develop near the valley of this interface due to the cool down process. There are some locations where compressive σ_{xx} and σ_{yy} are also observed which means that if there is a crack at this location, it will be arrested or crack surfaces will come into contact. Normal stresses calculated along the interfaces of the TGO are shown in Figure 34, produced by transforming σ_{xx} , σ_{yy} , σ_{xy} components into the normal stresses using equation 9. As can be seen from this figure, normal stresses calculated along both interfaces are a mirror image of each other with respect to a horizontal axis located at $\sigma = 0.25$ Gpa. It can also be seen that, normal stresses that develop on the lower interface (Bond Coat/TGO interface) are higher than the normal stresses that develop on the upper interface (TGO/Top Coat interface). The peak value of the normal stress is observed near the valley of the lower interface, therefore, this location is the most likely crack initiation site (assuming there is no other weaker plane located anywhere else in the specimen), see Figure 34.

$$\alpha_1 = \sin\theta, \quad \alpha_2 = \cos\theta$$

$$\sigma_{nn} = \sigma_{xx} \alpha_1 \alpha_1 + \sigma_{yy} \alpha_2 \alpha_2 - 2\sigma_{xy} \alpha_1 \alpha_2 \quad (9)$$

As an extension of this work, and considering the weak cleavage planes along the TGO/bond coat interface, an interface crack has been introduced at the location where this maximum stress exists.

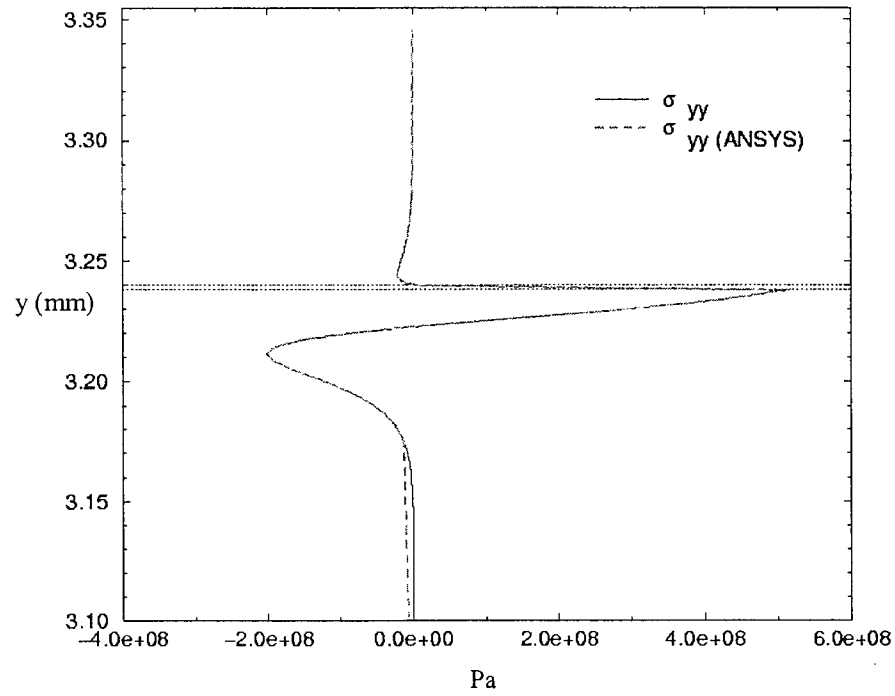


Figure 31: Variation of σ_{yy} along vertical axis for $x=0$.

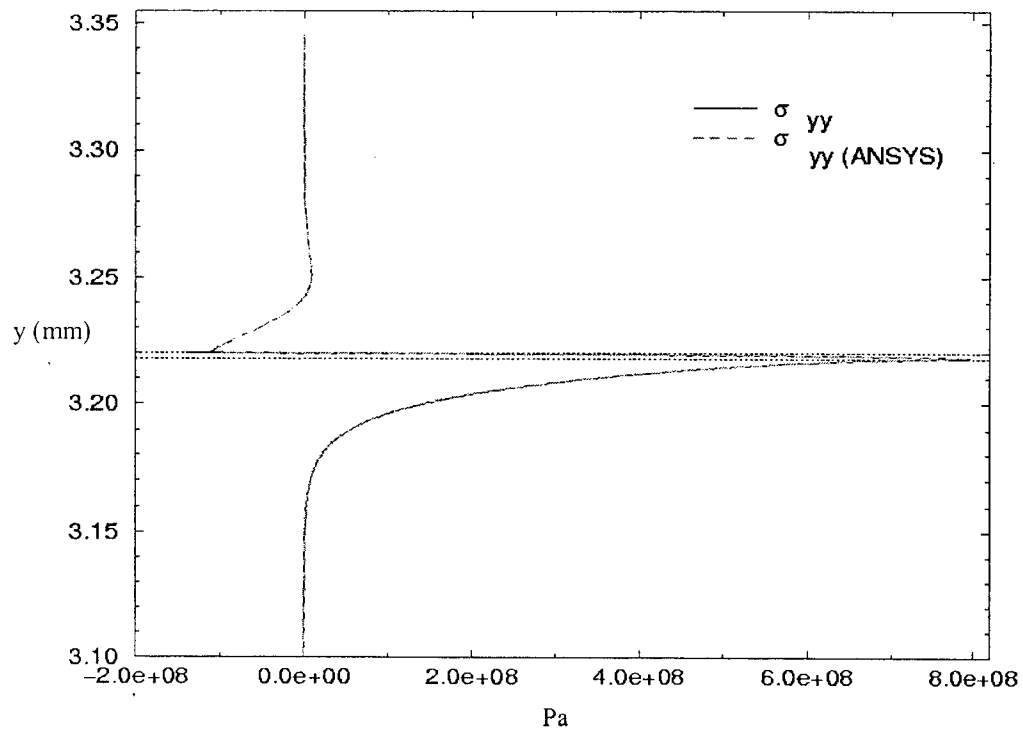


Figure 32: Variation of σ_{yy} along vertical axis for $x=0.025$ mm.

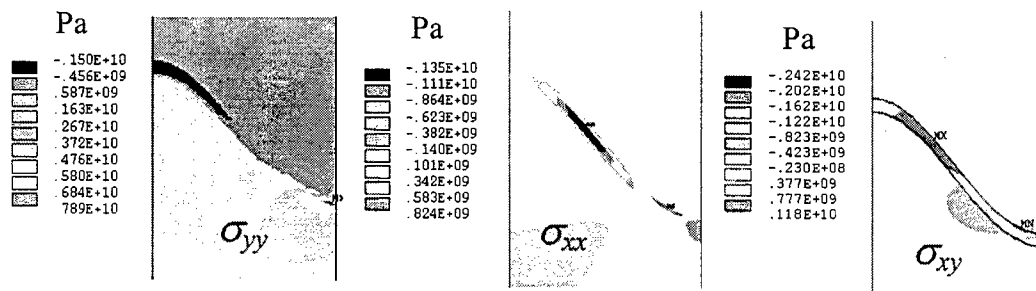


Figure 33: Stress contour plots on the slice after the specimen cools down to ambient temperature.

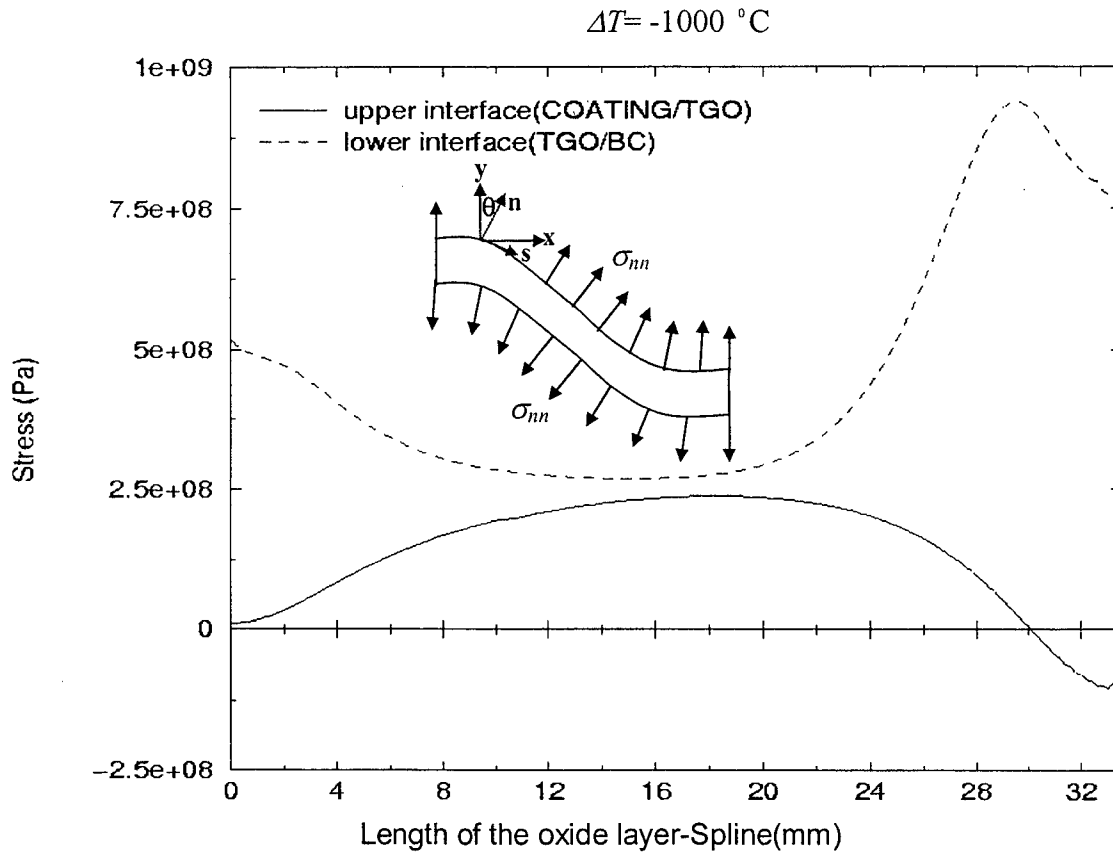


Figure 34: σ_{nn} , normal stresses on both interfaces of oxide layer.

7. Finite element modeling of a TBC slice with a crack located at the bottom interface of the TGO (Undulating TGO/Bond Coat interface and both edges are constrained horizontally)

An interface crack was introduced between TGO/bond coat interface as shown in Figure 35. Again $\Delta T = -1000\text{ }^{\circ}\text{C}$ is the only nonvanishing applied load. The crack length was varied along the interface and strain energy release rates were calculated. Typical finite element models with different crack lengths are shown in Figures 36, 37. It can be seen from Figure 36 that, as the crack propagates along this interface, there is opening

near the crack tip but closing at the point where crack has started from. Eventually, after a certain crack length, crack surface contact is observed around this point as shown in Figure 37. The overlapping of crack surfaces is a sign of contact and is not physically possible. Therefore this must be prevented either using a contact algorithm or node coupling, that is, letting the vertical displacements of nodes tied to each other. Node coupling along the contact surfaces was used in this problem. Contact occurred near the minimum point of the valley and tying of a few node displacements on almost a flat line near the minimum point of the curve was enough to solve the contact problem. Vertical displacements of the penetrating nodes, though unknown, are set to be equal to each other. Setting only vertical displacements equal to each other automatically assumes frictionless contact. Like most contact algorithms, node coupling also requires an iteration scheme and this was done manually as follows; First, without considering the contact, a calculation is performed and the deformed shape is examined to determine penetrated node pairs. Then the pair with the greatest penetration is coupled and another calculation is performed. Again penetration of any other node is checked, if there are others, the nodes with the greatest displacement differences are chosen and these nodes are coupled. This coupling continues until all surface node penetration is prevented along the crack faces. A deformed finite element mesh obtained this way is shown in Figure 38. The phase angles obtained from this analysis are shown in Figures 39. These quantities are plotted as a function of the crack tip location which is a measure for crack length but if one wants to find the actual crack length on the wavy interface, Equation 10 can be numerically integrated. This is a mixed mode problem due to the interface crack. It can be seen from this curve that as the

crack length is increased along the interface, the phase angle also increases and reaches a maximum. After a certain crack length is reached, it starts to decrease.

$$a = \left\{ \begin{array}{l} \int_0^x \left(1 + \left(\frac{\pi h}{L} \right)^2 \sin^2 \left(\frac{\pi t}{L} \right) \right)^{1/2} dt, \text{ for a crack starting from LHS} \\ \int_0^{L-x} \left(1 + \left(\frac{\pi h}{L} \right)^2 \sin^2 \left(\frac{\pi t}{L} \right) \right)^{1/2} dt, \text{ for a crack starting from RHS} \end{array} \right\} \quad (10)$$

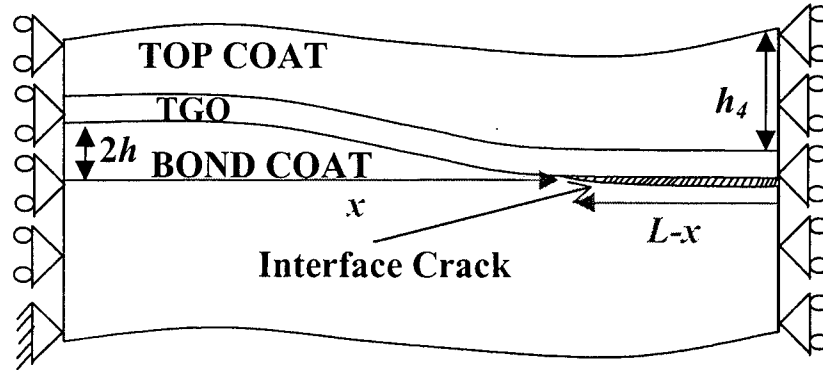


Figure 35: Geometry used in modeling the interface crack at TGO/BC interface.

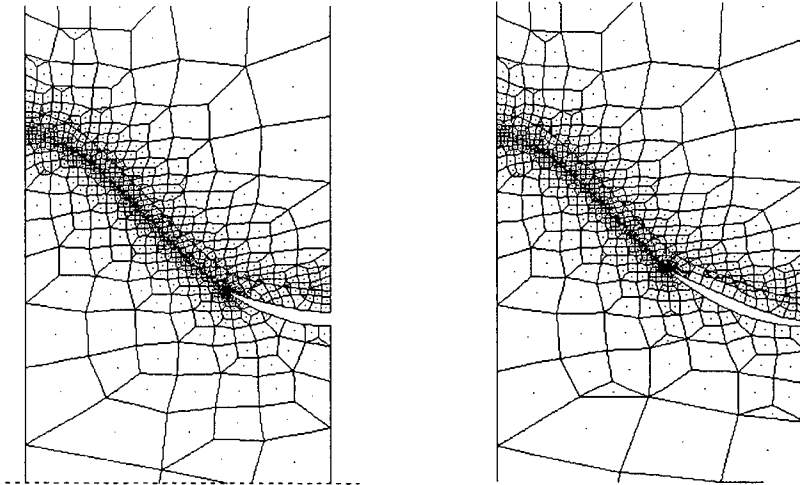


Figure 36: Typical deformed finite element models used in this analysis, scale=10.

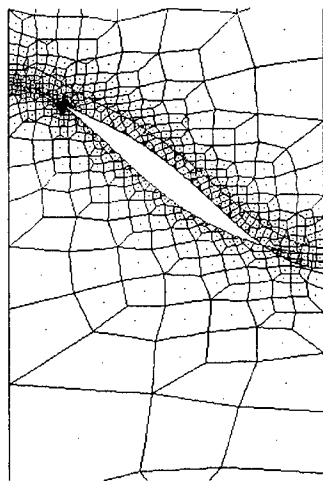


Figure 37: Deformed mesh without considering the crack surface contact, scale=10.

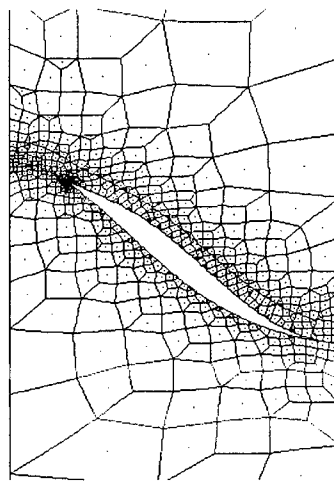


Figure 38: Deformed mesh considering the crack surface contact (node coupling used), scale=10.

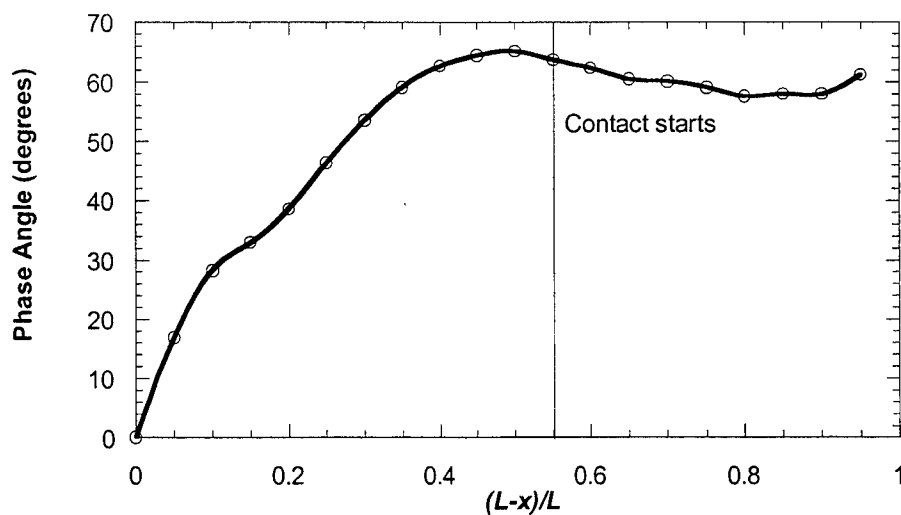


Figure 39: The phase angle vs. the crack tip location along the thickness of the TBC slice.

Even though the crack contact occurs when the crack length is greater than half thickness of the slice, this is not obvious from these curves. The phase angle smoothly continues to decrease. The reason for this smooth continuation can be attributed to the location of the contact, which is on the right hand side and far away from the crack tip. Therefore this contact zone does not have a very big effect on these fracture parameters (i.e. the contact zone is not close enough to cause a jump in these curves).

8. Weakened Interface Model and Determination of Theoretical Spring Constant for a TBC with a Crack at an Undulating Bond Coat/TGO interface (both edges are constrained horizontally)

Due to cool down, planar compressive stresses within a generic brittle layer (Ceramic and TGO) can lead to buckling, provided there is an interfacial crack already present between the TGO and metal substrate. Rather than a single large crack, there may be a weakened interfacial zone which consists of a series of small cracks with unbroken ligaments between $-a$ and a acting as springs (see Figure 40). For the buckling to occur, there is a critical load that must be reached (this is the thermal load in TBCs). It was shown that this critical load is a strong function of the theoretical spring constant in [12]. In this study, this constant will be determined as a function of crack length for cracks at an undulating bond coat/TGO interface. The same TBC-slice-model with a crack at undulating bond Coat/TGO interface was studied as in Section 7. In this case, the applied load is a uniform tensile stress along the surface of the top coat. As a result of this uniformly applied stress, displacements were calculated along the top surface as a function of crack length. The partially cracked TGO, bond coat interfacial region is

assumed to behave like a spring in vertical direction as the uniform tensile load is applied to the surface of the top coat. The magnitude of the applied stress is fixed and the crack length is the only variable. Geometry and a typical mesh used in this study are shown in Figures 41 and 42. Results obtained from this analysis are shown in Figures 43 and 44. In Figure 43, the vertical axis shows the theoretical spring constant and the horizontal axis shows the varying crack length along the undulating interface. Here one must be careful about displacement difference $(\Delta_1 - \Delta_0)$, where Δ_1 is the displacement calculated for the current crack length and Δ_0 is the displacement calculated from the model without a crack. In the model, the displacement on the top surface varies slightly along the thickness direction but this variation is only in the 5th digit. Therefore, the displacement at the mid-node is used in calculation of the spring constant. From Figure 43 it can be seen that as the crack length is increased the spring constant decreases and the decrease is very sharp. This is an interesting result, because this sharp decrease means that our spring softens, and the spring constant becomes very small with a small increase in the crack length. It is also shown in [12] that spring constant is proportional to the critical buckling load. Therefore it can be seen from this figure that with a little increase in the crack length, critical buckling load could decrease considerably. For small crack lengths, this constant is very high which means that critical buckling load is also very high which in turn makes this ceramic coating hard to buckle. Strain energy release rates obtained from this analysis are shown in Figure 44. As can be seen from this figure, there is a increase in the strain energy release rates with increasing interface crack length. Details on this weak interface model can be found in reference [12].

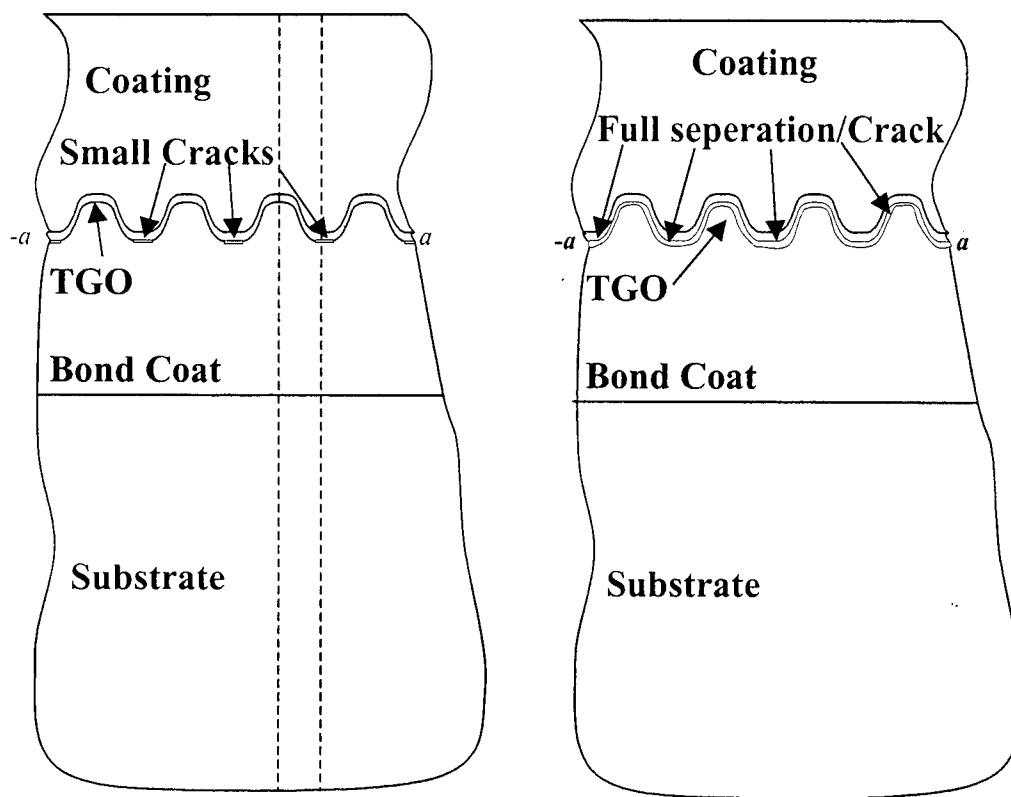


Figure 40: Weak interface model with a series of cracks and unbroken ligaments and full separation/crack model.

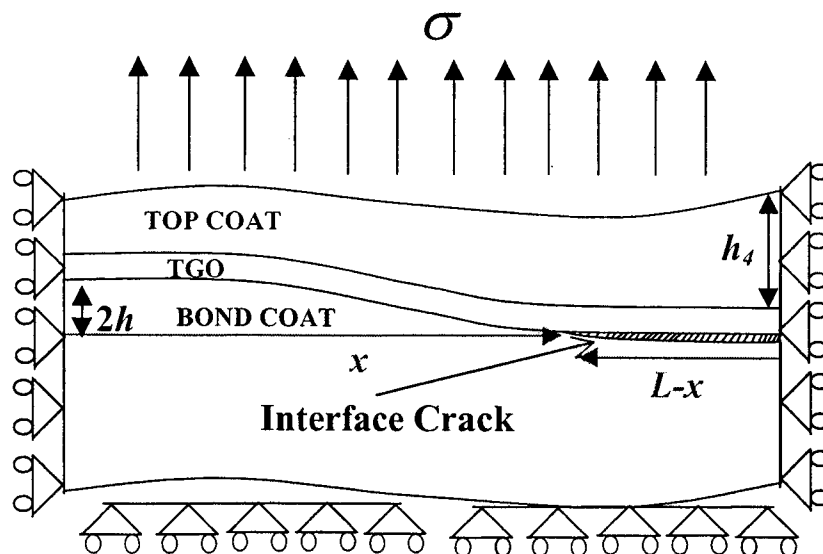


Figure 41: Geometry used in calculating the theoretical spring constant of the TBC with an interface crack at undulating TGO/BC interface.

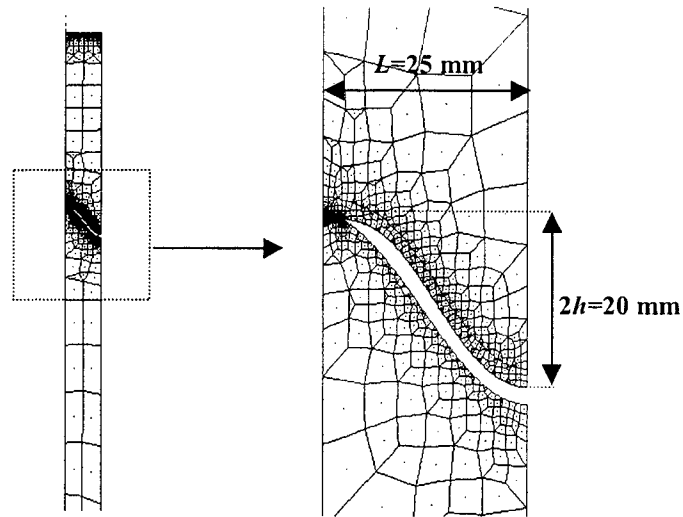


Figure 42: A typical finite element mesh used in calculating the theoretical spring constant for periodic interface cracks along the undulating TGO/BC interface, scale=10.

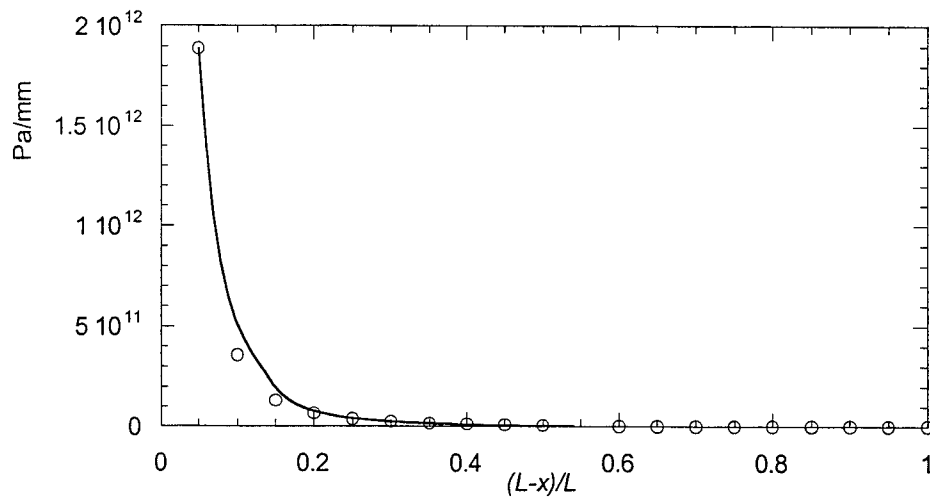


Figure 43: Theoretical spring constant vs. crack tip location.

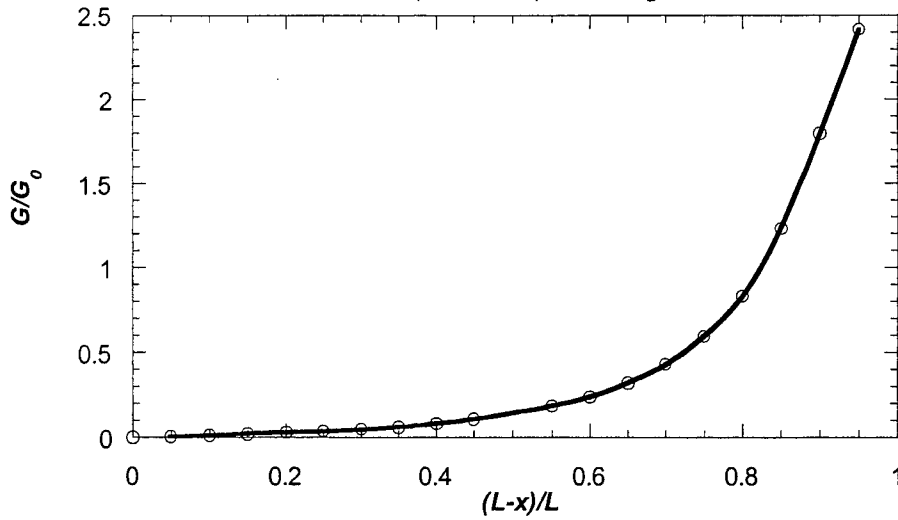


Figure 44: The strain energy release rates vs. crack tip location along the thickness of the TBC slice, $K_0 = \sigma \sqrt{\pi h_4}$, $G_0 = (1 - \nu_s^2) \frac{K_0^2}{E_s}$.

9. Stress Calculations in TBCs Using Undulating Oxide Model (one edge constrained horizontally with the other edge constrained to move with a constant, but unknown, horizontal displacement)

Applying a fixed horizontal constraint to both ends of the slice used in Section 6 may not be realistic. It simulates a TBC placed between two rigid blocks which may result in excessive stresses due to the large constraints on both ends. As an extension of the work done in Section 6, the same model is developed using ANSYS. In this model, one edge of the slice is allowed to deform horizontally. An additional constraint is that, the nodes along the right edge are tied to each other, i.e., they can deform horizontally but this horizontal displacement must be the same for all nodes located along this edge. The nodes are not constrained to deform vertically. The finite element model developed using ANSYS is shown in Figure 45. Loading is uniform temperature drop.

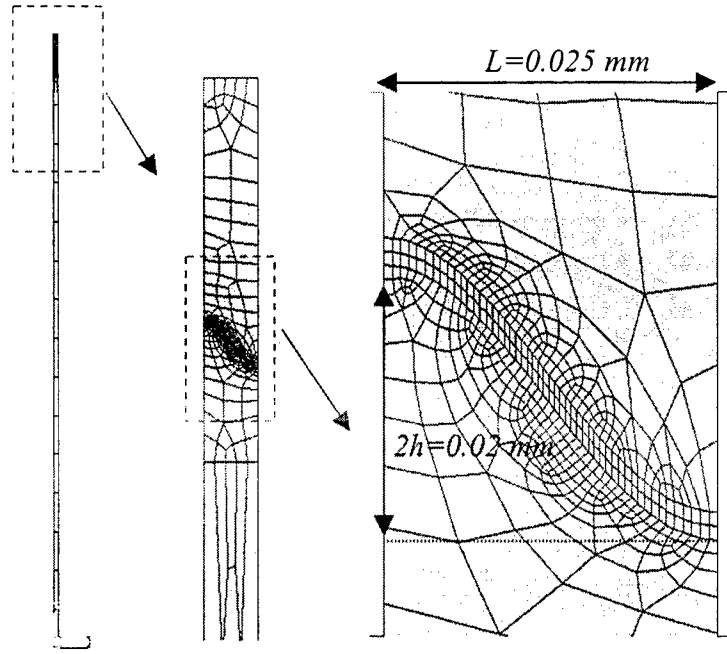


Figure 45: ANSYS model used in undulation problems, $L/h=25/10$.

Normal stresses and shear stresses computed along the Bond Coat/TGO and the TGO/Top coat interfaces are shown in Figure 46 obtained by using Equations 9 and 11.

$$\alpha_1 = \sin\theta, \quad \alpha_2 = \cos\theta$$

$$\sigma_{nt} = \sigma_{xy}(\alpha_2\alpha_2 - \alpha_1\alpha_1) + (\sigma_{yy} - \sigma_{xx})\alpha_1\alpha_2 \quad (11)$$

It can be seen from this figure that the normal stress along Top Coat/TGO interfaces is very small compared to the stress along bond coat/TGO interface. Therefore, bond coat /TGO interface is the critical interface for crack initiation. It can also be seen from this figure that the highest normal stress occurs at the peak of the rough interface. This conclusion is different than the one arrived in Section 6 which showed the maximum stress location near the valley of the rough interface. Contour plots of the stresses are shown in Figure 47. It can also be seen from these plots that the maximum stress is at the peak of the interface. Loading is uniform temperature drop in this problem.

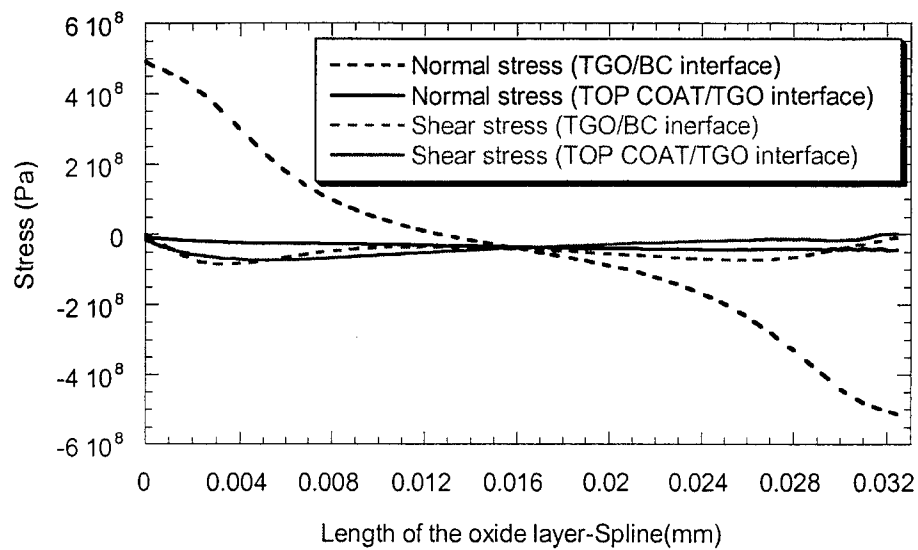


Figure 46: Normal and shear stresses σ_{nn} and σ_{ns} along the interfaces of the oxide layer.

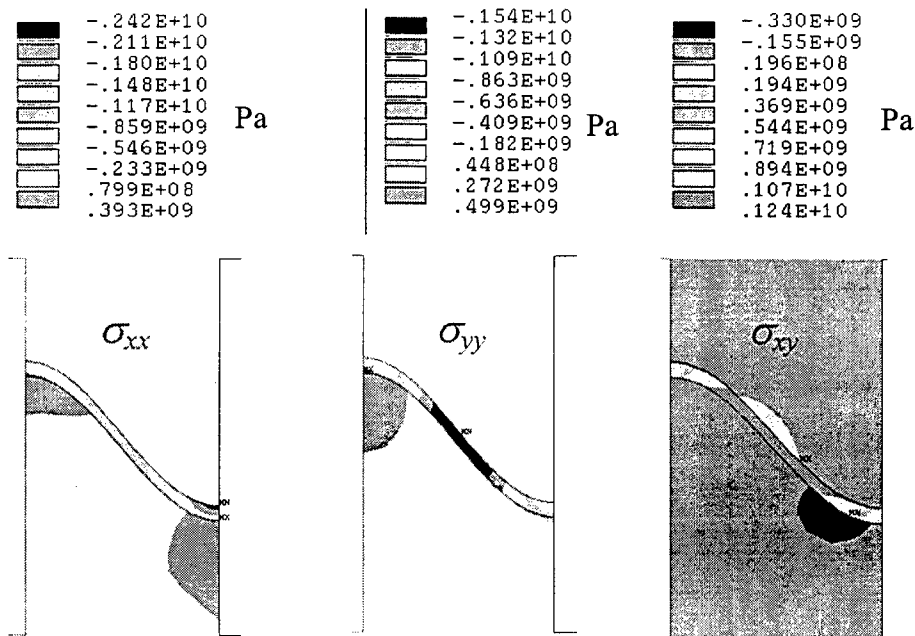


Figure 47: Stress contour plots on the slice after the specimen cools down to ambient temperature.

10. Stress Calculations in TBCs Using Undulating Oxide Model (one edge constrained horizontally and the other edge is free to have a rigid unknown rotation and horizontal displacement)

Tying horizontal nodal displacements for all of the nodes along one edge of the slice may also place too much constraint on the edge of the slice if the geometry is relatively thin. In reality, this is a unit cell strip taken from the TBC (see Figure 30). Therefore, this edge is rigid should be permitted to undergo a rigid rotation so that plane sections remain plane. To simulate this condition, a new geometry was created adjacent to the previous model. This is a simple bar, but the elastic modulus of this bar is very high and thermal expansion constant is set to zero. This rigid bar is “glued” to the previously existing geometry in such a way that, the nodes along the edge of the slice are free to move in x-direction with this rigid, newly created bar. The displacements along the axis of the bar are not constrained. This condition simulates the rigid rotation along the edge of the slice where new model and old model are aligned together. The model used in ANSYS is shown in Figure 48. Again $\Delta T = -1000^\circ\text{C}$ is the only nonvanishing applied load. The deformed mesh after the load is applied is shown in Figure 49. Since thermal extension coefficient of this rigid artificial bar is zero, there is no change in the dimension of the bar as can be seen from this figure. Horizontal displacements along the edge that is next to this artificial rigid bar are shown in Figure 50. It can be seen from this figure that there is a rotation along the edge of the slice because there is a linear variation in the horizontal displacement from bottom to the top corner of the edge. Again, normal stresses and shear stresses were computed along the interfaces of TGO by using equations 8 and 9. The results are shown in Figure 52. They seem not to be affected by

this condition, i.e, the results are the same as those calculated using tied boundary conditions allowing no rotation. The only difference is near the edge where the slice edge and the artificial bar are joined. Therefore assuming a tied boundary condition with no constraint in x -direction seems to be adequate for the solution of this particular problem.

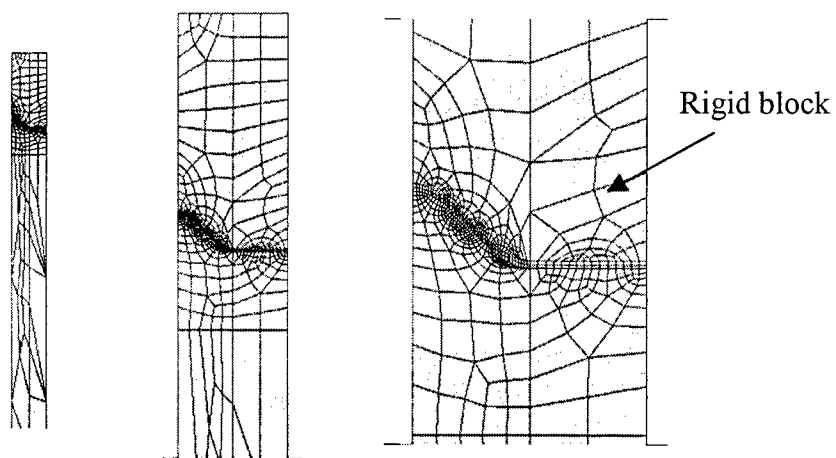


Figure 48: ANSYS mesh used in modeling of rigid rotation of the slice edge.

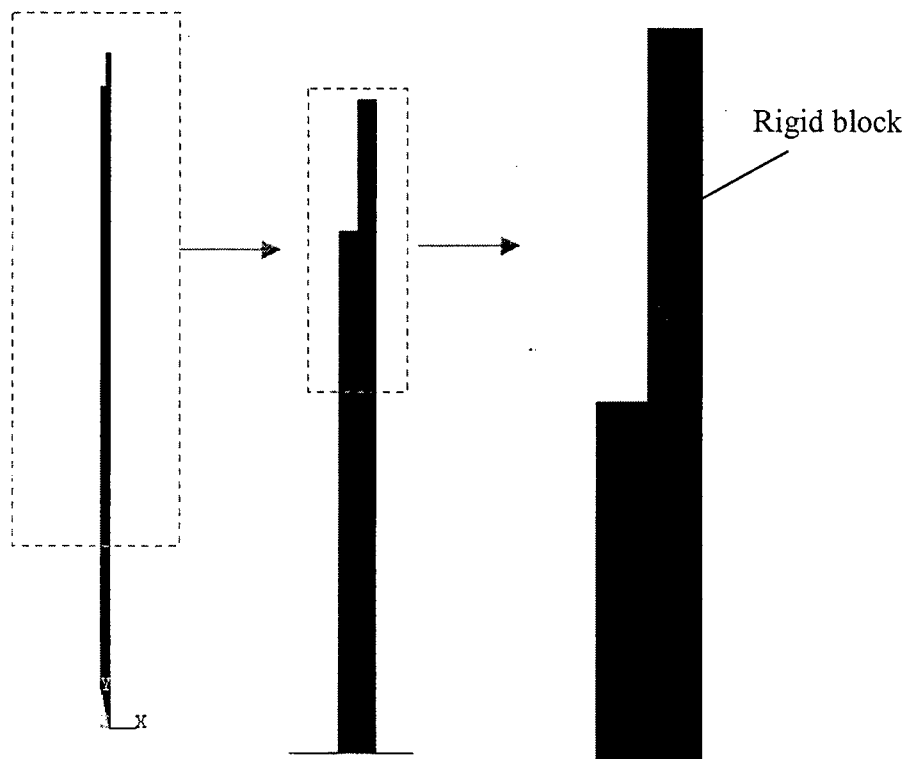


Figure 49: Deformed ANSYS mesh of the slice, there is no deformation in the rigid block.

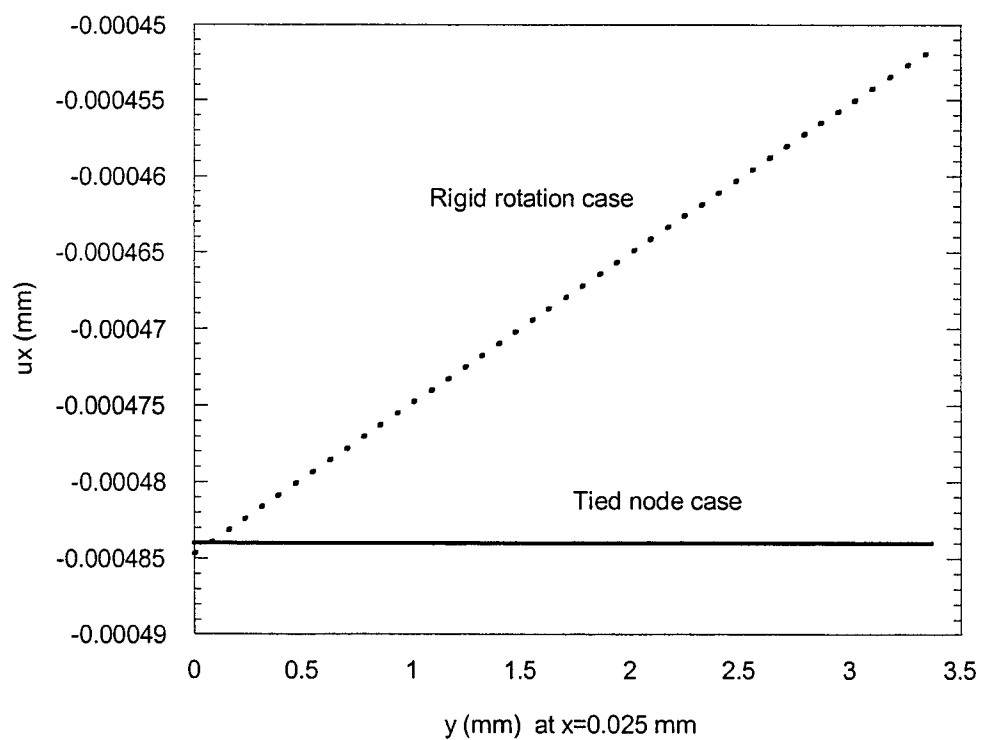


Figure 50: Horizontal displacement along the edge that is allowed to rotate.

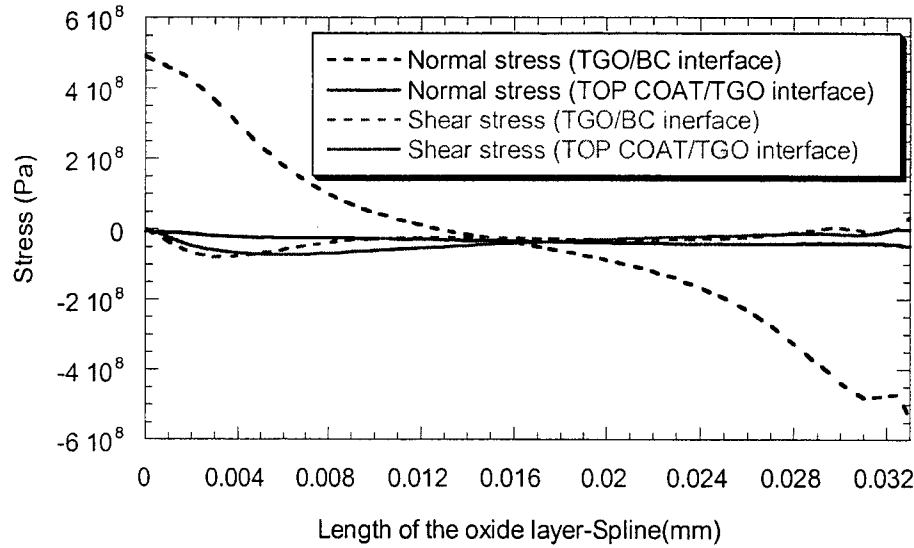


Figure 51: Normal and shear stresses σ_{nn} and σ_{ns} along the interfaces of the oxide layer.

11. Finite Element Modeling of a TBC Slice With a crack located at the bottom interface of the TGO (Undulating TGO/Bond Coat interface), one edge horizontally fixed and the other free to have a constant (unknown) horizontal displacement

An interface crack was introduced between the TGO/bond coat interface as shown in Figure 53. Again $\Delta T = -1000^\circ\text{C}$ is the only nonvanishing applied load. The crack length is varied along the interface and the strain energy release rate is calculated. Typical finite element models with different crack lengths are shown in Figure 53. It can be seen from Figure 52 that, as the crack propagates along the interface, starting from the left hand side of the specimen the maximum normal stress is observed at the peak of the rough interface. Nodes along the left edge of the slice are horizontally constrained and nodes along the right edge are tied, i.e. free to have the same unknown horizontal

displacement. The strain energy release rate calculated in this manner, is shown in Figure 54.

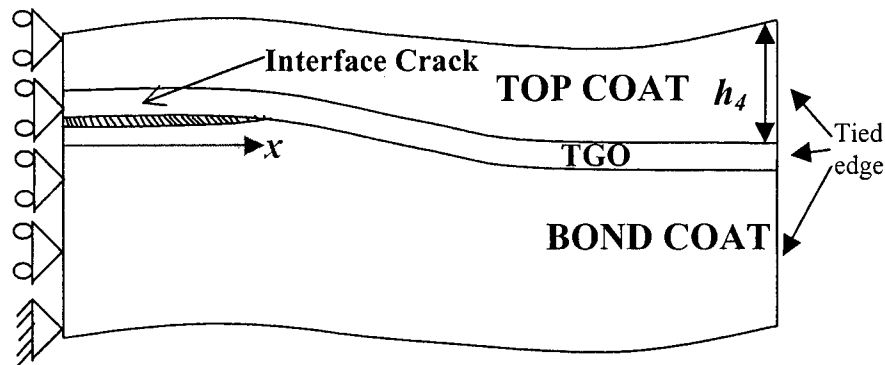


Figure 52: Geometry used in modeling the interface crack at TGO/BC interface.

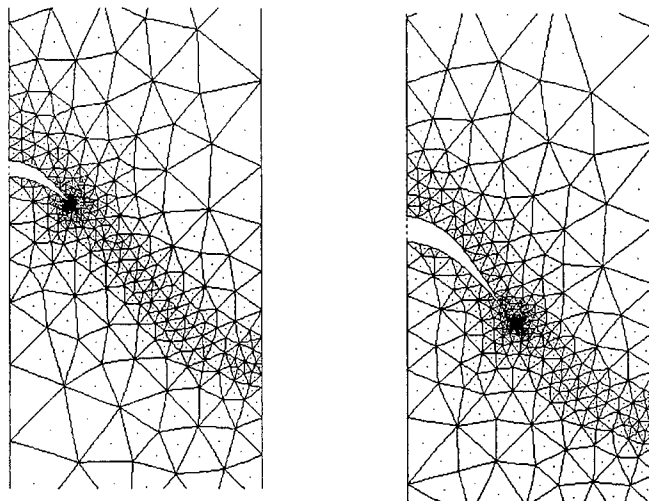


Figure 53: Two typical deformed finite element models used in this analysis, scale=10.

For small crack lengths the strain energy release rate is small and increases with increasing crack length. (The magnitudes are also close but this case seems to produce slightly higher strain energy release rates.) After the crack length reaches some value (which is the half length of the spline interface) , contact is observed. This contact is near the crack tip and cannot be solved simply by tying nodes as was done in Section 7.

Therefore, calculations were performed only until crack contact was observed. Calculated phase angles are shown in Figure 55. It can be seen from this figure that with increasing crack length, the absolute value of the phase angle increases and this increase is almost linear. The comparison of figure 55 and 39 shows a sign change, in this case the phase angles are always negative whereas in the previous case they were positive for all crack lengths.

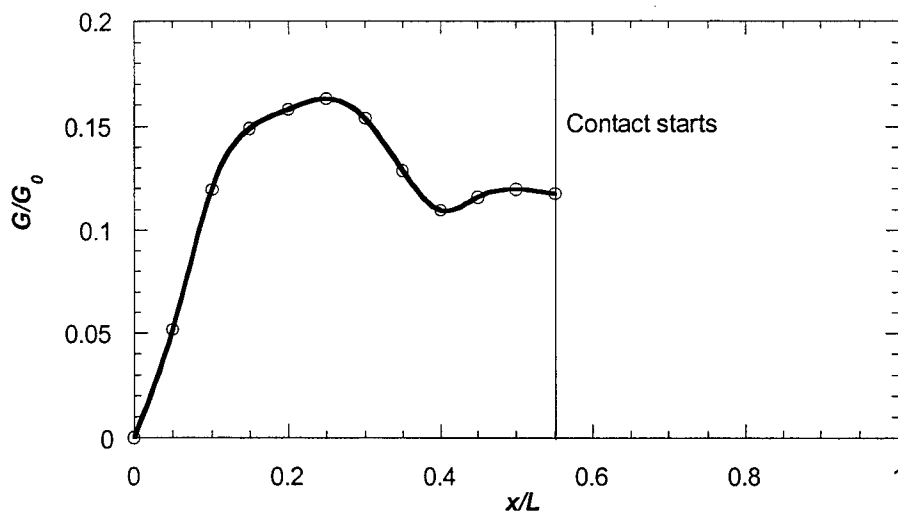


Figure 54: The strain energy release rate vs. crack tip location along the thickness of the TBC slice, $K_0 = E_s \alpha_s \Delta T \sqrt{\pi h_4}$, $G_0 = (1 - \nu_s^2) \frac{K_0^2}{E_s}$.

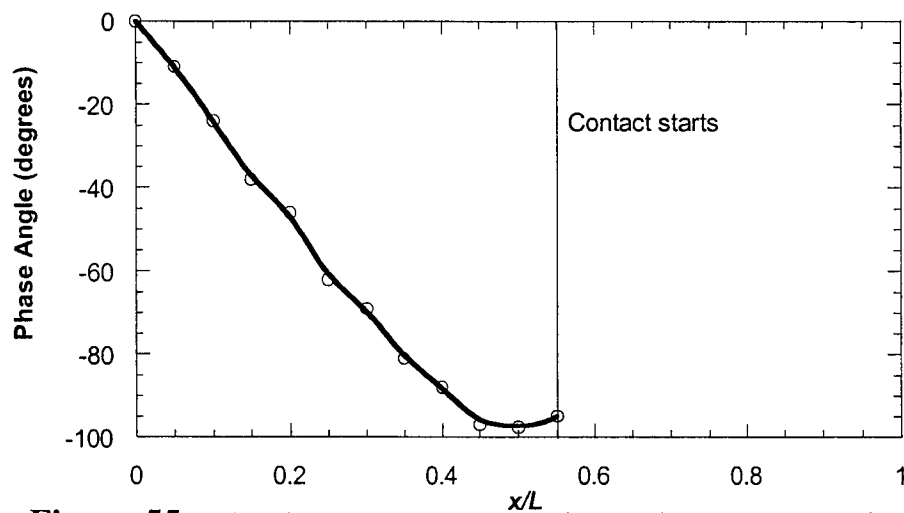


Figure 55: The phase angle vs. crack tip location along the thickness of the TBC slice.

12. Determination of the Theoretical Spring Constant for a TBC with a Crack at an Undulating Bond Coat/TGO interface, one edge is horizontally fixed and the other is free to have a constant (unknown) horizontal displacement

The TBC which consists of top coat, TGO and bond coat with an interface crack at the TGO/bond coat interface is assumed to behave like a spring in the vertical direction as the uniform tensile load is applied to the surface of top coat. Again, the magnitude of the applied stress is fixed and the only variable is the crack length. The geometry and a typical mesh used in this problem are shown in Figures 56 and 57.

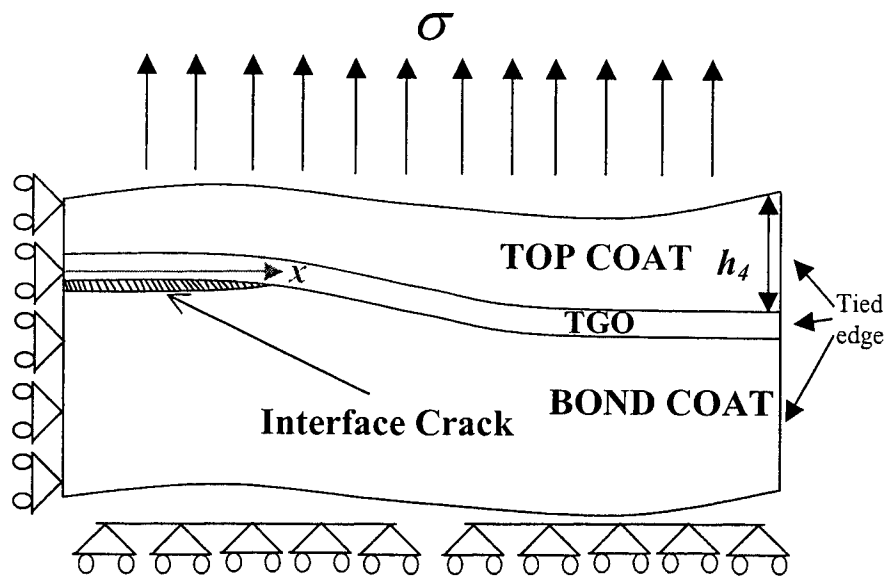


Figure 56: Geometry used in calculating theoretical spring constant of the TBC with an interface crack at undulating TGO/BC interface.

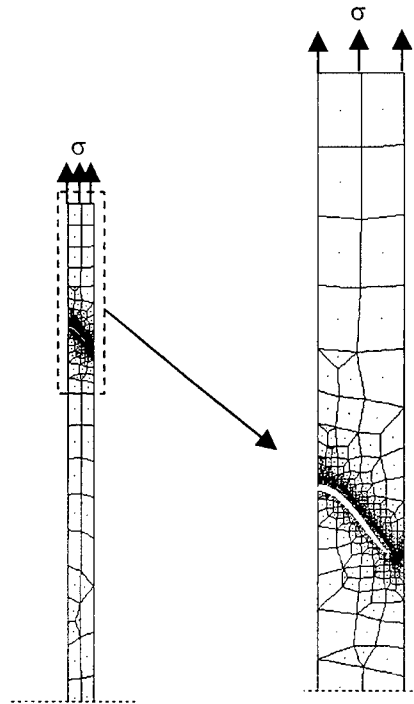


Figure 57: A typical finite element mesh used in calculating theoretical spring constant of the TBC with an interface crack at undulating TGO/BC interface, scale=10.

The difference between this study and the study done in Section 8, is the constraint applied to the right edge of the slice and the location of the crack. The right edge is tied in this study, i.e., can deform horizontally but the entire edge must have the same unknown horizontal displacement. As it was also shown in Section 9, the maximum normal stress occurs at the peak point of TGO/bond coat interface after cool down. Therefore, the peak of the TGO/BC interface is the most likely crack initiation site during processing. For this reason, in this part of the study, a model crack was started from the peak point, from the left hand side of the slice. Figure 58 shows the theoretical spring constant versus crack tip location. Again there is a sharp decrease in the spring constant with increasing crack length. The comparison of this figure with Figure 43

shows that the decrease is sharper when the both ends are constrained. The strain energy release rate versus crack tip location is shown in Figure 59. It can be seen from this figure that the strain energy release rate increases with increasing crack length. The comparison of figures 59 and 44 shows that for small crack lengths, the specimen with tied boundary conditions produces higher strain energy release rates than the fully constrained specimen.

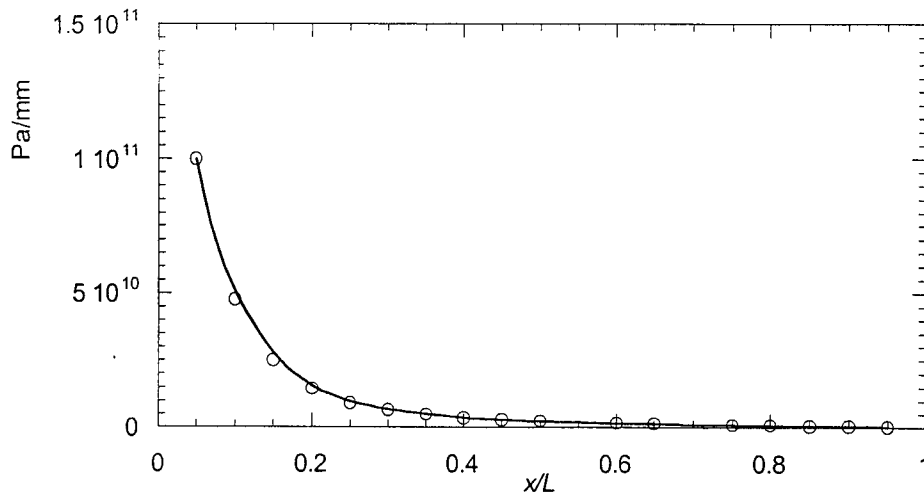


Figure 58: The theoretical spring constant vs. crack tip location along the thickness of the TBC slice.

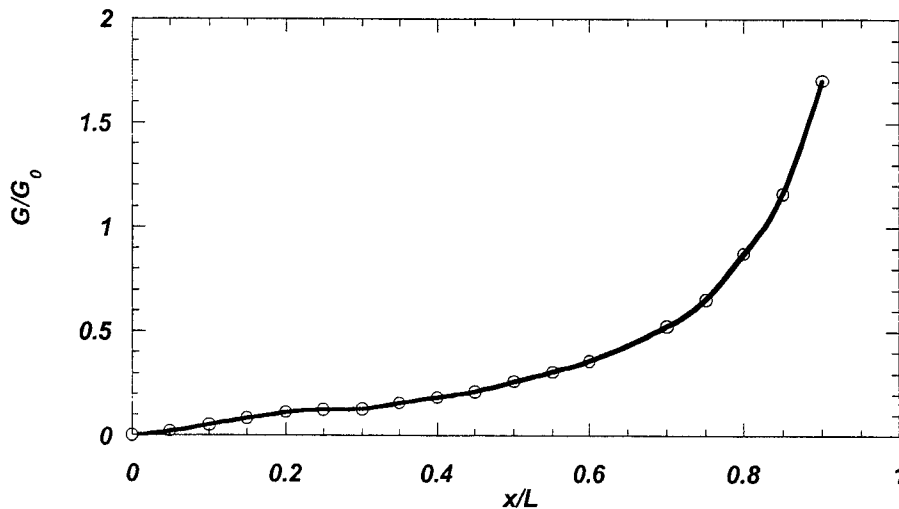


Figure 59: The strain energy release rate vs. crack tip location along the thickness of the TBC slice, $K_0 = \sigma \sqrt{\pi h_4}$, $G_0 = (1 - \nu_s^2) \frac{K_0^2}{E_s}$.

REFERENCES

- [1] S.M. Meier, D. M. K.D. Nissley, K. D. Sheffler and T. A. Cruse, "Thermal Barrier Coating Life Prediction Model Development, " *Journal of Engineering for Gas Turbine and Power*, Trans. ASME, MD-Vol 44, (1993) pp. 266-271.
- [2] B.D. Choules and K.Kokini, Multilayer Ceramic Coating Architecture Against Surface Thermal Fracture, Proceedings of the Symposium on ed. *Ceramic Coatings*, K. Kokini, E.d., ASME, MD.-Vol 44, (1993), pp.73-86.
- [3] M. Yamanaouchi, M.Koizumi, T. Hirai and I. Shiota (eds.) *FGM-90*, Proceedings of the First International Symposium on Functionally Graded Materials, FGM forum, Tokyo, Japan (1990) pp 197-202.
- [4] J. B. Holt, M. Koizumi, T.Hirai and Z. A. Munir (eds.) Proceedings of the Second International Symposium on Functionally Graded Materials, *Ceramic Transactions*, Vol. 34, American Ceramic Society, Westerville, Ohio (1993).
- [5] B. Ilschner and N. Cherradi (eds.) Proceedings of the Third International Symposium on Structural and Functional Gradient Materials, Presses Polytechniques et Universitaires Romandes, Lausanne, Switzerland (1995).
- [6] Functionally Gradient Materials, MRS Bulletin, Vol. 20, No.1 (1995).
- [7] Y. D. Lee and F. Erdogan, "Residual\Thermal Stresses in FGM and Laminated Thermal Barrier Coating," *International Journal of Fracture*, Vol. 69 (1995) pp. 145-165.
- [8] K. Kurihara, K. Sasaki and M.Kawarada, "Adhesion Improvement of Diamond Films," in *FGM-90*, Yamanouchi et. Al. (eds.) (1990) pp. 65-69.

- [9] A. C. Kaya and H. F. Nied, "Interface Fracture Analysis of Bonded Ceramic Layers Using Enriched Finite Elements," MD-Vol. 44, *Ceramic Coatings* ASME (1993) pp 47-71.
- [10] S. Q. Nusier and G. M. Newaz, "Analysis of Interfacial Cracks in a TBC/Superalloy System Under Thermo-mechanical Loading, " to appear in j. of Engineering fracture mechanics.
- [11] E. P. Chen, "Finite Element Analysis of a Bimaterial Interface Crack," Theoretical and Applied Fracture Mechanics, vol. 3, (1985), pp. 257-262.
- [12] T.Z. Chiu and F. Erdogan "Buckling of Graded Coatings "AFOSR Technical Report, Lehigh University, October 2000.
- [13] J.T. DeMasi, K.D. Sheffler and M. Ortiz, "Thermal Barrier Coating Life Prediction Model Development", Phase I-II Final Report, December 1989.
- [14] S. Q. Nusier, G. Newaz, "Crack Initiation in Thermal Barrier Coatings Due to Interface Asperity", Proceedings of The Eight Japan-U.S. Conference on Composite Materials., (1998), pp 417-426.